



Goethe Universität Frankfurt am Main

Fachbereich 13

Institut für Theoretische Physik

BACHELOR THESIS

---

Heavy Spin Effects in the  $\bar{b}bud$ ,  $I(J^P) = 0(1^-)$   
Tetraquark Resonance in the  
Born-Oppenheimer Approximation

---

*Author:*

Jakob Hoffmann

*Supervisors:*

Prof. Dr. Marc Wagner  
Prof. Dr. Owe Philipsen

Submitted on  
October 14, 2024


## Selbständigkeitserklärung

Ich versichere hiermit, dass ich die vorliegende Arbeit selbständig verfasst und keine anderen als die angegebenen Quellen und Hilfsmittel verwendet habe.

Alle Stellen und Textpassagen, die wörtlich oder sinngemäß aus veröffentlichten Quellen oder anderen fremden Texten entnommen sind, sind als solche kenntlich gemacht. Ebenso wurden alle Abbildungen, sofern nicht selbst von mir erstellt, mit entsprechenden Quellennachweisen versehen.

Diese Arbeit wurde noch nicht, auch nicht auszugsweise, für eine andere Studien- oder Prüfungsleistung verwendet.

\_\_\_\_\_  
Datum

  
\_\_\_\_\_  
Unterschrift

# Abstract

In this thesis I study heavy spin effects in the  $\bar{b}b u d$  tetraquark system with quantum numbers  $I(J^P) = 0(1^-)$ . In my approach I use antistatic-antistatic-light-light potentials calculated from lattice QCD. With these potentials, I derive a coupled-channel Schroedinger equation, where heavy spin effects manifest in the mass splitting between  $B$  and  $B^*$  mesons. Furthermore, I make use of a two-channel scattering formalism to describe the system for energies above threshold. I use this formalism to derive relations to calculate the T matrix. In a numerical study, I investigate the existence of a tetraquark resonance by searching for T matrix poles in the complex energy plane. Motivated by the results of this study, I conclude that heavy quark spins have a significant impact on the four-quark system and cannot simply be neglected in future studies of this kind. At the end of this thesis I also provide an outlook on possible improvements and next steps.

# Contents

<b>1</b>	<b>Introduction and Motivation</b>	<b>1</b>
<b>2</b>	<b>Theoretical Formalism</b>	<b>3</b>
2.1	Born-Oppenheimer Approximation . . . . .	3
2.2	Static Potentials from Lattice QCD . . . . .	4
2.3	Coupled-Channel Schroedinger Equation . . . . .	6
2.3.1	Fierz-Identities . . . . .	6
2.3.2	Formulating the Hamiltonian . . . . .	7
2.4	Blocks with Total Spin $\mathbf{S}$ . . . . .	8
2.5	Symmetries and Quantum Numbers . . . . .	11
<b>3</b>	<b>Coupled-Channel Scattering</b>	<b>14</b>
3.1	Emergent Wave Method . . . . .	14
3.2	Boundary Conditions and T Matrix . . . . .	16
3.3	Coupled-Channel Phase Shifts . . . . .	17
3.4	Riemann Sheets and Analytical Structure . . . . .	18
3.4.1	General Definition . . . . .	18
3.4.2	Single-Channel . . . . .	18
3.4.3	Two Channels . . . . .	20
3.5	Numerical Method . . . . .	21
<b>4</b>	<b>Numerical Results</b>	<b>24</b>
4.1	Numerical Procedure and Error Analysis . . . . .	24
4.1.1	Numerical Procedure and Input Parameters . . . . .	24
4.1.2	Error Analysis . . . . .	24
4.2	Pole Search in the Complex Plane . . . . .	25
4.2.1	Rotating the potential matrix . . . . .	26
4.2.2	Unphysical Heavy Quark Mass . . . . .	28
4.3	Branching Ratios . . . . .	29
4.4	Coupled-Channel Eigenphases . . . . .	31
<b>5</b>	<b>Conclusion and Outlook</b>	<b>33</b>
<b>A</b>	<b>Dimensionless Quantities</b>	<b>34</b>
<b>B</b>	<b>Conservation of Orbital Angular Momentum</b>	<b>35</b>
<b>C</b>	<b>Derivation of the Unitarity Constraint</b>	<b>37</b>
<b>D</b>	<b>Convergence of Branching Ratios</b>	<b>39</b>
	<b>Acknowledgements</b>	<b>40</b>
	<b>Bibliography</b>	<b>41</b>

*Dedicated to my parents Agata Hoffmann, Jędrzej Hoffmann*

## Chapter 1

# Introduction and Motivation

In the last decade a new interest in studying the properties of exotic states in QCD has emerged. Experimental measurements like [1] revealed a new range of possible candidates for exotic bound states and resonances. Exotic states are states that cannot be described in terms of a simple meson or baryon quark combination. One type of such exotic states are tetraquark states which consist of a SU(3) color neutral combination of two quarks and two antiquarks. Recent experimental studies at LHCb, Belle and BESII ([1–21]) have proven them to be likely candidates for the description of states like the  $X(3872)$  or the recently discovered  $T_{cc}^+$ . The majority of these exotic four-quark states falls under the domain of heavy-light tetraquarks and are located in the high-energy nonperturbative QCD spectrum. In recent history there has been an ongoing effort from the theoretical side to explain exotic states such as the  $T_{cc}^+$ . In this light many different theoretical descriptions([22–80]) were developed which make use of tools from lattice QCD, effective field theory and phenomenological models.

The framework of lattice QCD offers a fully relativistic numerical evaluation of problems in QCD at low energy scales. Since its first formulation by Wilson ([81]) in the early 70's, lattice QCD has enabled a variety of new studies in many different areas of high-energy physics. One formidable milestone was the study of hadron masses that can be only calculated with non perturbative QCD. In modern applications lattice QCD is continuously being used to push boundaries in the physics of form factors(see [82–100]), nuclear physics (see [101–118]), multiparticle scattering (see [119–126]) and many other areas. The formalism of lattice QCD is also suited to handle four-quark systems. In works such as [22–37, 74–80] the Lüscher method, a method to obtain scattering amplitudes from two particle spectra via the two-particle quantization condition (QC2) was utilized to predict  $\bar{b}b\bar{u}d$  and  $\bar{b}bus$  tetraquark bound states. Such full lattice QCD studies provide, in principle reliable results which can be compared to experimental observations. However, the computational effort required for such studies for even only a few ensembles is sizable and needs to be gauged accordingly to provide any meaningful results in a limited amount of time. A good compromise to avoid the computational resources of lattice studies and still retain most of the physical significance are effective field theory models. Effective field theories mostly introduce approximations to simplify the study of a particular system. For qualitative studies effective field theories such as non-relativistic QCD(NRQCD) or potential non-relativistic QCD(pNRQCD) are sufficient and can produce results close to experiment as shown by works such as [41–71]. The Born-Oppenheimer approximation is an example for such an effective field theory and provides a practical framework to study heavy-light four-quark states in a non-relativistic setup by using the static quark approximation for heavy  $b$ - or  $c$ -quarks.

This work focuses on the study of four-quark states with a  $\bar{b}b\bar{u}d$  quark composition in the Born-Oppenheimer approximation. First studies of a  $\bar{b}b\bar{u}d$  tetraquark bound state with quantum numbers  $I(J^P) = 0(1^+)$ , also known as the  $T_{bb}$  were conducted in 2012 by M.Wagner et al. ([61]). These studies were later extended to resonances. In [64, 65] clear signal for a p-wave resonance with quantum numbers  $I(J^P) = 0(1^-)$  with real energy  $\text{Re}(E) = 17_{-4}^{+4}$  MeV and width  $\Gamma = 112_{-103}^{+90}$  MeV was found. In all of these studies effects due to the spin of the heavy  $\bar{b}$ -quarks and due to spin-orbit interactions were neglected. However, in a realistic setup these effects are important and must be considered. In [63] heavy spin effects were incorporated through the mass splitting between the  $B$  and the  $B^*$  mesons. The value of this mass splitting  $m_{B^*} - m_B \approx 45$  MeV, taken from experiment, suggests that heavy spin effects play a sizable role in the systems behavior. This was confirmed by studies of the  $\bar{b}b\bar{u}d$  four-quark state with quantum numbers  $I(J^P) = 0(1^+)$  ([63]), where heavy spin effects were included. The resulting binding energy showed a decrease of  $\mathcal{O}(40)$  MeV compared to the study without heavy spin effects contained in [72]. The resonance pole found in [64, 65] has a real part of the energy close to the  $BB$  threshold, therefore it is questionable whether the resonance pole found in [64,

[65] persists when including heavy spin effects which effectively reduce the total attraction between the quark composites. The main motivation for this work is to extend the formalism developed in [63] to scattering states in order to include heavy spin effects into the resonance search for the  $I(J^P) = 0(1^-)$  four-quark state conducted in [64, 65]. The theoretical formalism presented in chapters 2 and 3 of this work is built upon a combination of the formalism developed in [63] and a coupled-channel scattering formalism similar to the one constructed in [54, 67, 70]. This formalism is used to conduct a numerical study. Results of this study are shown in chapter 4. At last, conclusions drawn from the results are discussed and an outlook on future steps is provided in chapter 5.

## Chapter 2

# Theoretical Formalism

Processes involving the strong interaction are described by the non-abelian theory of Quantum Chromo Dynamics (QCD) in the Standard model of particle physics. At high energy quarks  $\psi_{c,f}$  and gluons  $A_\mu^a$  are asymptotic free ([127]) and perturbation theory is valid. For low energies  $E \approx \Lambda_{QCD}$  with  $\Lambda_{QCD} \approx 150\text{MeV}$  the coupling constant takes values of order 1, leading to a breakdown of perturbation theory. Typically in hadron physics one is interested in these low energy scales for which one has to instead rely on other methods such as effective field theories or numerical evaluations via lattice calculations. In principle with lattice methods one can solve the full QCD theory but this requires a lot of computational effort and time. For qualitative statements about a particular system it might be sufficient to use an effective field theory description instead. Effective field theories are designed to give an order by order approximation to the full theory. For example, for systems consisting of heavy and light particles it is useful to remove the dynamics of the heavy particles by separating the heavy and light degrees of freedom and expand the whole theory in orders  $\mathcal{O}(1/m_{\text{heavy}})$ , where  $m_{\text{heavy}}$  is the mass of the heavy particle. One possibility is to use the Born-Oppenheimer approximation for heavy quarks. In this section a short summary of the Born-Oppenheimer approximation applied to antiheavy-antiheavy-light-light tetraquarks is given. In this section I also recapitulate some of the methods first proposed in [63].

### 2.1 Born-Oppenheimer Approximation

The main philosophy behind any effective field theory is to a priori perform a separation of scales. The Born-Oppenheimer approximation is an example for a non relativistic effective field theory. For a comprehensive discussion on the Born-Oppenheimer approximation as an effective field theory, I recommend to check out [128]. In the Born-Oppenheimer approximation light degrees of freedom are separated from the heavy degrees of freedoms of a given system. In the context of antiheavy-antiheavy-light-light tetraquarks this implies a separation between the two antiheavy and the two light quarks (this is shown in **Figure 2.1**). The heavy quarks are approximated as static. The interactions of the light quarks are fully described by the static potential between the heavy quarks. The remaining interaction between the heavy quarks is treated as a multi-body problem within the framework of non-relativistic quantum mechanics. Correspondingly, there are two major steps, when treating an antiheavy-antiheavy-light-light tetraquark ( $\bar{Q}\bar{Q}qq$ ) system in the Born-Oppenheimer approximation.

- 1) Calculating static potentials which contain effects from the light quarks using tools from lattice QCD
- 2) Solving a coupled-channel stationary Schroedinger equation between the heavy quarks  $\bar{Q}$  to look for bound states and resonances

Noticeably, the only part where actual Lattice Field theory calculations are needed is step 1), whereas step 2) is completely independent of the relativistic physics of Quantum field theory. Evidently, the approximation breaks down if there is no clear separation between static and dynamic degrees of freedom. This is true for four-quark states which are composed out of only light quarks or fully heavy tetraquarks. For these systems other approaches are more well suited. However, for systems involving two  $\bar{b}$ - and two light quarks it appears to be a feasible assumption to use the static approximation for the  $\bar{b}$ -quarks since their mass  $m_b \approx 4180\text{MeV}$



([129]) is large compared to the light quark scales of the system. For these systems there is a clear separation of scales and the Born-Oppenheimer approximation is applicable.

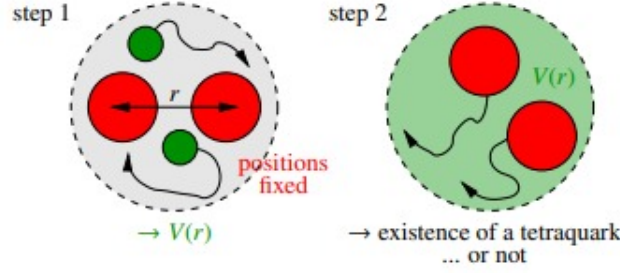


**Figure 2.1:** Graphic picture of the two steps of the Born-Oppenheimer approximation in a tetraquark system. The static potential is denoted by  $V(r)$ .

## 2.2 Static Potentials from Lattice QCD

Lattice QCD is one of the main tools for numerical computations in the field of hadron spectroscopy. The existing literature on this topic is broad. Here, I summarize only the basic concepts needed to compute potentials between two static antiquarks. The basic idea of lattice QCD is to discretize the spacetime domain. Let  $\Lambda \subset \mathbb{R}^3$  denote a three dimensional cubic lattice. Let further  $G$  be a Lie group with corresponding Lie algebra  $\mathfrak{g}$ . In lattice QCD gauge field components  $A_\mu \in \mathfrak{g}$  with  $\mu \in [1, 4]$  over the Lie-algebra  $\mathfrak{g}$  are replaced by components of link variables  $U_\mu \in G$ . Gauge links and gauge fields are related by an exponential map<sup>1</sup>. The discretization of fermionic fields is more involved and requires more care. A naive discretization leads to 15 additional unphysical fermions which are called "doublers". There are many existing approaches on how to circumvent this problem. Most of them can be found in [130]. In hadron spectroscopy, the main observables are two-point correlation functions  $C(t)$  constructed out of a suitable base of operators  $O$ . The choices for  $O$  must reflect the quantum numbers of the state. These operators are used to compute temporal correlation functions between two points in time. The general expression for the two-point correlation function  $C(t)$  for operators with fixed spatial position  $\vec{r}$  in the path integral formalism after integrating out all fermionic fields  $\psi_f, \bar{\psi}_f$  with flavor  $f$  becomes

$$\begin{aligned} C(t) &= \langle O(t, \vec{r}) O^\dagger(0, \vec{r}) \rangle = \frac{1}{Z} \int DU \prod_f D\bar{\psi}_f D\psi_f O(t, \vec{r}) O^\dagger(0, \vec{r}) e^{-S_{\text{QCD}}[\psi_f, \bar{\psi}_f, U]} \\ &= \frac{1}{Z} \int DU \prod_f \det(D_f) \langle O(t, \vec{r}) O^\dagger(0, \vec{r}) \rangle_U e^{-S_{\text{gauge}}[U]}, \end{aligned} \quad (2.1)$$

where  $U \in \Gamma(\Omega^1(\Lambda; SU(3)))$  is a one-form that describes gauge links over the group  $SU(3)$ ,  $S_{\text{QCD}}$  is the full QCD action,  $S_{\text{gauge}}$  is the pure-gauge part of the QCD action and  $D_f$  is the Dirac operator corresponding to flavor  $f$ . The average  $\langle \dots \rangle_U$  denotes the expectation value on a particular gauge link  $U$ . This average can be calculated by considering all possible Wick contractions between the quark fields contained in the operator  $O$  and the quark fields contained in  $O^\dagger$ . The set of all possible operators  $O$  is simplified, when fixing the heavy quarks to be infinitely heavy (see [63]). In the static approximation the fermion determinant is typically set to  $\det(D_f) = 1$  for heavy quarks  $f \in \{b, c\}$ . Moreover, in this limit Wick contractions only need to be performed between light quark fields.

In [63] it was shown that the most general structure for four quark operators describing an antiheavy-antiheavy-light-light four-quark state with isospin  $I = 0$  in the static approximation is

$$O_{\mathbb{L}, \mathbb{S}}(\vec{r}_1, \vec{r}_2) = (\mathbb{C}\mathbb{L})_{\alpha\beta} (\mathbb{C}\mathbb{S})_{\gamma\delta} (\bar{Q}_\gamma^a(t, \vec{r}_1) u_\alpha^a(t, \vec{r}_1)) (\bar{Q}_\delta^b(t, \vec{r}_2) d_\beta^b(t, \vec{r}_2)) - (u \leftrightarrow d), \quad (2.2)$$

where  $\vec{r}_1, \vec{r}_2$  denote the positions of the static  $\bar{b}$  quarks,  $a, b \in [1; 3]$  are spinor-color indices,  $\alpha, \beta, \gamma, \delta \in [1; 4]$  are spin indices,  $\mathbb{C} = \gamma_4 \gamma_2$  is the charge conjugation matrix,  $\gamma_j$  is the  $j$ th gamma matrix and  $\mathbb{L}, \mathbb{S}$  are the light quark and heavy quark spin matrices. The matrices  $\mathbb{L}$  and  $\mathbb{S}$  are elements of the 16-dimensional

<sup>1</sup>Let  $X \in \mathfrak{g}$  and  $\gamma : \mathbb{R} \rightarrow G$  be a curve with tangent vector  $X$  at the identity, then the exponential map is defined as  $\exp : \mathfrak{g} \rightarrow G, \exp(tX) = \gamma(t), t \in \mathbb{R}$

Clifford algebra with euclidean metric  $D$ , where  $D_{ij} = \delta_{ij}$ ,  $i, j \in [1; 4]$ , denoted by  $C\ell(\text{spin}, D)$ . The light quark spin matrix  $\mathbb{L}$  and the heavy quark spin matrix  $\mathbb{S}$  are chosen such that the trial states  $O_{\mathbb{L}, \mathbb{S}}^\dagger |\Omega\rangle$  have definite quantum numbers  $|j_z\rangle$ ,  $\mathcal{P}$  and  $\mathcal{P}_x$ , where  $|j_z\rangle$  is the total angular momentum of the light quarks and gluons along the separation axis of the heavy antiquarks,  $\mathcal{P}$  denotes parity and  $\mathcal{P}_x$  the behavior under reflection along an axis which is perpendicular to the separation axis. In [63] angular momenta  $|j_z\rangle \in \{0, 1\}$  were considered. For this there are 16 possible choices for the light quark spin matrix  $\mathbb{L} \in \{(1 \pm \gamma_0)\mathbb{1}, (1 \pm \gamma_0)\gamma_5, (1 \pm \gamma_0)\gamma_j, (1 \pm \gamma_0)\gamma_5\gamma_j\}$ . For the heavy quark spin matrix there are only 8 possible choices  $\mathbb{S} \in \{(1 + \gamma_0)\mathbb{1}, (1 + \gamma_0)\gamma_5, (1 + \gamma_0)\gamma_j, (1 + \gamma_0)\gamma_5\gamma_j\}$  because static quark spinors have only two components instead of 4. In section 2.3, I show that different choices for  $\mathbb{L}$  and  $\mathbb{S}$  can be interpreted in terms of different combinations of  $B, B^*, B_0^*, B_1^*$  mesons. In the following only the lightest mesons, i.e. the pseudoscalar  $B$  and the vector  $B^*$  are considered. The spin matrices associated with these mesons are  $\mathbb{L} \in \{(\mathbb{1} \pm \gamma_0)\gamma_5, (\mathbb{1} \pm \gamma_0)\gamma_j\}$  and  $\mathbb{S} \in \{(\mathbb{1} + \gamma_0)\gamma_5, (\mathbb{1} + \gamma_0)\gamma_j\}$ .

In the static approximation the spins of the heavy quarks are irrelevant. In this limit  $B$  and  $B^*$  mesons have degenerate masses, thus all static potentials will have the same asymptotic values  $2m_{B^{(*)}}$ , where  $m_{B^{(*)}}$  is the  $B^{(*)}$  meson mass. The heavy spin matrix  $\mathbb{S}$  can thus be chosen arbitrarily in the lattice computation. Static potentials differ in the choice of the light quarks spin matrix. For each choice of the light quark spin matrix  $\mathbb{L}$  there is one fixed color combination of light quarks. The two light quarks can be either in a triplet  $\bar{\mathbf{3}}$  or a sextet  $\mathbf{6}$ , leading to two correlation functions  $C_{\mathbb{L}}(t)$ .

For large euclidean time  $t \rightarrow \infty$  the correlation functions  $C_{\mathbb{L}}$  can be expanded in an energy spectrum  $\{E_n\}_{n \in \mathbb{N} \cup \{0\}}$  of a Hilbert space  $\mathcal{H}$  via the spectral decomposition

$$C_{\mathbb{L}}(t) = \sum_{n=0}^{\infty} |\langle n | O_{\mathbb{L}}^\dagger | \Omega \rangle|^2 e^{-E_n t} = \sum_{n=0}^{\infty} Z_{n, \mathbb{L}} e^{-E_{n, \mathbb{L}} t}, \quad (2.3)$$

where  $Z_{n, \mathbb{L}} := \langle n | O_{\mathbb{L}}^\dagger | \Omega \rangle$  is the overlap factor of an energy eigenstate state of order  $n$  with the state described by the operator  $O_{\mathbb{L}}$ . The overlap factor is a measure for how well a particular trial state  $O_{\mathbb{L}}^\dagger | \Omega \rangle$  describes an energy eigenstate  $|n\rangle$ .

At large  $t \rightarrow \infty$  the spectrum of the two-point correlation function  $C(t)$  is dominated by the ground state with energy  $E_{0, \mathbb{L}}$  up to exponentially negligible corrections from excited states

$$C_{\mathbb{L}}(t) = Z_{0, \mathbb{L}} e^{-E_{0, \mathbb{L}} t} \left( 1 + \mathcal{O} \left( e^{(E_{0, \mathbb{L}} - E_{1, \mathbb{L}}) t} \right) \right), \quad t \rightarrow \infty. \quad (2.4)$$

For fixed positions of the static quarks  $\vec{r}_1, \vec{r}_2$  in equation (2.2), the static potential  $V_{\mathbb{L}}(r)$ , where  $r = |\vec{r}_1 - \vec{r}_2|$  is the separation distance between the  $\bar{b}$  quarks, can be calculated from the ground state energy  $E_{0, \mathbb{L}}$  as.

$$V_{\mathbb{L}}(r) = E_{0, \mathbb{L}} |_{r=|\vec{r}_1 - \vec{r}_2|}. \quad (2.5)$$

In [72] two potentials for isospin  $I = 0$  were calculated. These include an attractive potential  $V_5(r)$  for  $\mathbb{L} = (\mathbb{1} + \gamma_0)\gamma_5$  and a repulsive vector potential  $V_j(r)$  for  $\mathbb{L} = (\mathbb{1} + \gamma_0)\gamma_j$ . In [72] it was further shown that the lattice data points for the static potentials  $V_X(r)$  can be consistently fitted to

$$V_X(r) = -\frac{\alpha_X}{r} e^{-(r/d_X)^2}, \quad X \in \{5, j\}. \quad (2.6)$$

The fit parameters  $\alpha_X$  and  $d_X$  denote the strength and the depth of the potential respectively. For the  $I=0$  potentials the values  $\alpha_5 = 0.34_{-0.03}^{+0.03}$ ,  $d_5 = 0.45_{-0.10}^{+0.12}$  fm and  $\alpha_j = -0.10 \pm 0.07$ ,  $d_j = (0.28 \pm 0.02)$  fm were determined in [72] via a  $\chi^2$  minimizing fit. Parametrized versions of the potentials  $V_5(r)$  and  $V_j(r)$  are depicted in **Figure 2.2**.

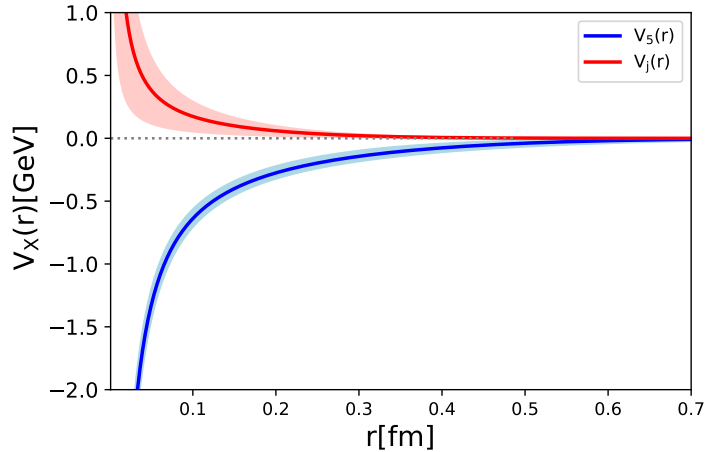


**Figure 2.2:** Parametrized lattice data of the potentials  $V_5$  and  $V_j$  for isospin  $I = 0$  as a function of the separation  $r$ .

For small separations  $r$ , the system is dominated by one-gluon exchange and perturbation theory is valid. In this region the potential has the shape of a coulomb potential and goes like  $1/r$  as shown in **Figure 2.2**. For large separations the potential is exponentially screened and dominated by interactions between meson pairs. This observation suggests a mapping between the operators  $O_{\mathbb{L},\mathbb{S}}$  defined in 2.2 and linear combinations of pairs of  $B$  and  $B^*$  mesons. The algebraic relations between the operators  $O_{\mathbb{L},\mathbb{S}}$  and pairs of  $B$  and  $B^*$  mesons are worked out in section 2.3.1.

### Higher order spin corrections

In the calculation of the static potentials effects originating from the heavy quark spin were completely neglected. This treatment would be accurate if we lived in a world, where bottom quarks are infinitely heavy. In real world calculations effects from heavy spin will always contribute. This leads to corrections to the static potentials. A systematic way to classify these corrections is provided by the framework of pNRQCD ([131]), where corrections are classified in orders of  $1/m_b$ , with  $m_b$  being the heavy quark mass. The pNRQCD Lagrangian in the multiple expansion reads ([132])

$$\mathcal{L} = -\frac{1}{4}F_{\mu\nu}^a F^{\mu\nu a} + \text{Tr} \left[ \psi^\dagger \left( iD_0 - \frac{\vec{p}^2}{m_b} - V_s^{(0)} - \sum_{n=1}^{\infty} \frac{V_s^{(n)}}{m_b^n} \right) \psi \right], \quad (2.7)$$

where  $F_{\mu\nu}^a$ ,  $a \in [1, 8]$  are the components of the gluon field-strength tensor,  $\psi$  is the heavy quark field,  $\vec{p}$  the heavy quark momentum and  $D_0$  the 0th order covariant derivative. The matching coefficients  $V_s^{(n)}$  correspond to order by order corrections to the static potentials. The coefficients  $V_s^{(n)}$  can be computed via correlation functions with field strength insertions( for more see [132]).

## 2.3 Coupled-Channel Schroedinger Equation

The second major step of the Born-Oppenheimer approximation is to formulate a non-relativistic Schroedinger equation with static potentials as input. In this section previously neglected heavy spin effects are included via the mass splitting between the  $B$  and  $B^*$  meson. This leads to a  $16 \times 16$  coupled channel Schroedinger equation, where each channel contains a particular combination of  $B$  and  $B^*$  mesons.

### 2.3.1 Fierz-Identities

The operators defined in (2.2) can be recast into linear combinations of meson-pairs by rearranging the quark fields with Fierz- identities.

**Theorem 1: Fierz-identities**

Let  $\bar{\psi}_1, \psi_2, \bar{\psi}_3, \psi_4 \in \text{spin}(3,1)$  be four dirac spinors and  $\Gamma_1, \Gamma_2 \in C\ell(\text{spin}, D)$  be elements of the Clifford algebra with euclidean metric  $D$ , then the following relation holds:

$$(\bar{\psi}_1 \Gamma_1 \bar{\psi}_3)(\bar{\psi}_2 \Gamma_2 \psi_4) = \sum_{\sigma \in \mathcal{S}_n} G(\sigma) (\bar{\psi}_1 \tilde{\Gamma}_1 \psi_2)(\sigma) (\bar{\psi}_1 \tilde{\Gamma}_2 \psi_2)(\sigma), \quad (2.8)$$

where  $G(\sigma) \in \mathbb{C}$  are prefactors that belong to some combination of bilinear structures with Clifford algebra elements  $\tilde{\Gamma}_1, \tilde{\Gamma}_2 \in C\ell(\text{spin}, D)$ .

Using Theorem 1 the operators defined in equation (2.2) can be expressed through heavy-light quark bilinears  $(\bar{Q}\Gamma^a\bar{q})$ , where  $\Gamma^a \in C\ell(\text{spin}, D)$  is a combination of dirac matrices. The following relation was derived in [63]

$$O_{\mathbb{L}, \mathbb{S}}(\vec{r}_1, \vec{r}_2) = \sum_{A, B \in [1;4]} G_{AB}(\mathbb{S}, \mathbb{L}) \left( \bar{Q}(\vec{r}_1) \tilde{\Gamma}^A q^{f_1}(\vec{r}_1) \right) \left( \bar{Q}(\vec{r}_2) \tilde{\Gamma}^B q^{f_2}(\vec{r}_2) \right), \quad (2.9)$$

where  $q^{f_1}, q^{f_2}$  are light quark fields of two different flavors  $f_1, f_2$  and the coefficients  $G_{AB}(\mathbb{S}, \mathbb{L})$  are uniquely determined through the relation

$$G_{AB}(\mathbb{S}, \mathbb{L}) = \frac{1}{16} \text{Tr} \left( (\mathbf{CS})^T \tilde{\Gamma}_A^T (\mathbf{CL}) \tilde{\Gamma}_B \right). \quad (2.10)$$

The values of dirac matrices  $\tilde{\Gamma}^A, \tilde{\Gamma}^B \in \{(\mathbb{1} + \gamma_0)\gamma_5, (\mathbb{1} + \gamma_0)\gamma_j\}$  reflect different heavy-light meson combinations, therefore the following abbreviations for the quark bilinears are introduced

$$\left( \bar{Q}(\vec{r}_i) \tilde{\Gamma}^A q^f(\vec{r}_i) \right) := \begin{cases} B(\vec{r}_i), & \text{if } \tilde{\Gamma}_A = (\mathbb{1} + \gamma_0)\gamma_5 \\ B_j^*(\vec{r}_i), & \text{if } \tilde{\Gamma}_A = (\mathbb{1} + \gamma_0)\gamma_j \end{cases}, \quad (2.11)$$

where  $j \in \{x, y, z\}$  denotes the cartesian spin orientation of the  $B^*$  meson. Henceforth, the position arguments of  $B$  and  $B^*$  mesons will be omitted whenever it is not necessary to write them out explicitly. Equation (2.9) allows one to map any operator with some specific light and heavy spin to the corresponding linear combination of mesons. Note, up to this point no concrete isospin  $I$  has been chosen. Definite isospin  $I$  emerges, when the light-quark flavors in equation (2.9) are either symmetrized ( $I = 1$ ) or antisymmetrized ( $I = 0$ ). Further details on the interpretation in terms of definite isospin, can be found in section 2.5.

### 2.3.2 Formulating the Hamiltonian

In [63] heavy spin effects were introduced via a mass splitting between the  $B$  and  $B^*$  mesons. This accounts for leading order corrections up to order  $1/m_b$  in the kinetic term of the pNRQCD expansion, where  $m_b$  is the bottom-quark mass. Higher order corrections in the static potentials starting from  $\mathcal{O}(1/m_b)$  are not contained in the formalism presented in this section. One way to include these additional contributions, would be an improved calculation of the potential by taking also spin-spin corrections on top of the static approximation into account as briefly addressed at the end of section 2.2. Based on [63], a Hamiltonian  $H$  that contains the mass splitting  $m_{B^*} - m_B \approx 45 \text{ MeV}$  ([133]) can be constructed. The free part of the hamiltonian  $H_0$  up to  $\mathcal{O}(1/m_b)$  is constructed by adding terms containing masses of  $B$  and  $B^*$  mesons unto the usual kinetic terms

$$H_0 := M \otimes \mathbb{1}_{4 \times 4} + \mathbb{1}_{4 \times 4} \otimes M + \frac{\vec{p}_1^2}{2m_b} \otimes \mathbb{1}_{16 \times 16} + \frac{\vec{p}_2^2}{2m_b} \otimes \mathbb{1}_{16 \times 16}, \quad (2.12)$$

where  $\vec{p}_1, \vec{p}_2$  are the  $\bar{b}$  momenta,  $m_b$  is the bottom quark-mass and  $M = \text{diag}(m_B, m_{B^*}, m_{B^*}, m_{B^*})$  is the mass matrix. The interacting part of the hamiltonian  $H_{\text{int}}$  containing the static potential potentials  $V_5$  and  $V_j$  reads

$$H_{\text{int}} = \mathbb{G} V \mathbb{G}^{-1}, \quad (2.13)$$

where  $V = \text{diag} \left( \mathbb{1}_{4 \times 4} \otimes V_5, \mathbb{1}_{12 \times 12} \otimes V_j \right)$  is a  $16 \times 16$  diagonal potential matrix,  $\mathbb{G} \in \mathbb{C}^{16 \times 16}$  is a  $16 \times 16$  transformation matrix with entries

$$\mathbb{G}_{\text{ind}(\mathbb{L})+4\text{ind}(\mathbb{S}); A+4B} = G_{AB}(\mathbb{S}, \mathbb{L}), \quad (2.14)$$

where  $\text{ind}(\mathbb{S}), \text{ind}(\mathbb{L}) = 0$  for  $\mathbb{L}, \mathbb{S} = (\mathbb{1} + \gamma_0)\gamma_5$  and  $\text{ind}(\mathbb{S}), \text{ind}(\mathbb{L}) = j$  for  $\mathbb{L}, \mathbb{S} = (\mathbb{1} + \gamma_0)\gamma_j$ . The Fierz coefficients  $G_{AB}(\mathbb{S}, \mathbb{L})$  were specified in equation (2.10). The components of  $\mathbb{G}$  can be found in [63]. The total Hamiltonian  $H := H_0 + H_{\text{int}}$  acts on a 16-component wave-function  $\vec{\Psi}_M \in L^2(\mathbb{R}^3, \mathbb{C}^{16})^2$  with  $M$  denoting pairs of  $B$  and  $B^*$  mesons, defining a  $16 \times 16$  Schroedinger equation

$$[H_0 + H_{\text{int}}] \vec{\Psi}_M = E \vec{\Psi}_M, \quad (2.15)$$

where  $E$  is the energy resulting of the eigenvalue problem of the hamiltonian  $H$ . The 16 components of the wave-function  $\vec{\Psi}_M$  corresponding to all combinations of  $B$  and  $B^*$  mesons are

$$\vec{\Psi}_M = \begin{pmatrix} BB \\ BB_x^* \\ \vdots \\ B_x^* B \\ B_x^* B_x^* \\ \vdots \\ B_z^* B_y^* \\ B_z^* B_z^* \end{pmatrix}. \quad (2.16)$$

Equations (2.15) are partial differential equations that contain in total 6 independent variables  $\vec{r}_1, \vec{r}_2$ . The static potentials in the interacting Hamiltonian depend only on the relative coordinates  $\vec{r} = \vec{r}_2 - \vec{r}_1$ . This motivates to perform a coordinate transformation to the center-of-mass frame, where only the relative coordinate  $\vec{r}$  is relevant. This effectively reduces the number of independent coordinates to the three relative coordinates  $\vec{r}$ . In the center of-mass frame  $m_b$  in the free Hamiltonian  $H_0$  must be replaced by the reduced mass  $\mu := m_b/2$ . The free Hamiltonian  $H_0$  then becomes

$$H_0 = M \otimes \mathbb{1}_{4 \times 4} + \mathbb{1}_{4 \times 4} \otimes M - \frac{1}{2\mu} \left[ \frac{\partial^2}{\partial r^2} + \frac{2}{r} \frac{\partial}{\partial r} - \frac{\mathbf{L}^2}{r^2} \right] \otimes \mathbb{1}_{16 \times 16}. \quad (2.17)$$

Here, another coordinate transformation was applied to write the laplacian  $\nabla^2$  in 3d spherical polar coordinates and the  $\theta$  and  $\varphi$ -derivatives were replaced by the squared angular momentum operator  $\mathbf{L}^2$  as found in standard textbooks on quantum mechanics. The corresponding coupled-channel Schroedinger equation then becomes

$$\left[ M \otimes \mathbb{1}_{4 \times 4} + \mathbb{1}_{4 \times 4} \otimes M - \frac{1}{2\mu} \left( \frac{\partial^2}{\partial r^2} + \frac{2}{r} \frac{\partial}{\partial r} - \frac{\mathbf{L}^2}{r^2} \right) \otimes \mathbb{1}_{16 \times 16} + H_{\text{int}} \right] \vec{\Psi}(\vec{r}) = E \vec{\Psi}(\vec{r}). \quad (2.18)$$

Even though equation (2.18) now only depends on three variables, it is still a set of 16 coupled partial differential equations. However, the amount of equations can be significantly reduced by considering the symmetries of the system which have not been included up to this point.

## 2.4 Blocks with Total Spin $\mathbf{S}$

The total spin  $\mathbf{S} := \mathbf{S}_q + \mathbf{S}_Q$  is a combination of the total light quark spin  $\mathbf{S}_q$  and the total heavy quark spin  $\mathbf{S}_Q$ . Furthermore, the orbital angular momentum  $\mathbf{L}$  is conserved. The reason for the conservation of  $\mathbf{L}$  is not trivial and related to spherical symmetry in the potentials  $V_5$  and  $V_j$ . In fact, one can show that  $[\mathbf{L}, H] = 0$  is fulfilled, only if the interaction Hamiltonian  $H_{\text{int}}$  depends exclusively on the radial coordinate  $r$ . An explicit proof can be found in appendix A. From the conservation of  $\mathbf{L}$  it also follows that the total spin  $\mathbf{S}$  must be conserved. The conservation of the total spin  $\mathbf{S}$  gives rise to a total spin quantum number  $S$  whose range of values is determined by combinations of the light quark spin quantum number  $S_q \in \{0, 1\}$  and heavy quark spin quantum number  $S_Q \in \{0, 1\}$ . This suggests a diagonalization of equation (2.15) into blocks labeled by  $S$ . Mathematically this is manifested in a decomposition of group products into irreducible representations via a Clebsch-Gordan decomposition.

<sup>2</sup>  $L^2(\mathbb{R}^3, \mathbb{C}^{16})$  denotes the space of all square integrable mappings  $f : \mathbb{R}^3 \rightarrow \mathbb{C}^{16}$

**Theorem 2: Clebsch-Gordan decomposition**

Let  $G$  be a finite dimensional Lie group. Let  $V_m$  and  $V_n$  be irreducible representations of  $G$  with weights  $w(V_m) = m$  and  $w(V_n) = n$ , then the product representation  $V_m \otimes V_n$  can be decomposed into a direct sum of irreducible representations according to:

$$V_m \otimes V_n \cong \bigoplus_{i=m-n}^{m+n} V_i. \quad (2.19)$$

Let further  $B(V_m) \subset V_m$  and  $B(V_n) \subset V_n$  be bases of  $V_m$  and  $V_n$  then a base  $B(V_1 \otimes V_2)$  of the product representation can be constructed as

$$B(V_m \otimes V_n) = \sum_{i,j=|w(V_m)-w(V_n)|}^{w(V_m)+w(V_n)} C(w(V_m), w(V_n); i, j) B(V_i) \otimes B(V_j), \quad (2.20)$$

where  $V_i$  and  $V_j$  are irreducible representations of  $G$  of weights  $i$  and  $j$ . The coefficients  $C(w(V_m), w(V_n); i, j)$  are commonly known as Clebsch-Gordan coefficients.

Definite quark spins are described by irreducible representations of  $SU(2)$ . Each quark spin is described by a doublet  $\mathbf{2} \in I(SU(2))$ , where  $I(SU(2))$  denotes the set of all irreducible representations of the group  $SU(2)$ . The spin structure of the four-quark state is a group product of four doublets. Using Theorem 2, this product can be decomposed as

$$\mathbf{2} \otimes \mathbf{2} \otimes \mathbf{2} \otimes \mathbf{2} = (\mathbf{1} \oplus \mathbf{3}) \otimes (\mathbf{1} \oplus \mathbf{3}) = \mathbf{1} \otimes \mathbf{1} + \mathbf{3} \otimes \mathbf{1} + \mathbf{1} \otimes \mathbf{3} + \mathbf{3} \otimes \mathbf{3} = \mathbf{2} \oplus \mathbf{9} \oplus \mathbf{5}. \quad (2.21)$$

The first part of equation (2.21), already worked out, contains the mapping between quark combinations to linear combinations of  $B$  and  $B^*$  mesons via Fierz identities. The spins and parities  $J^P$  of the  $B$  and  $B^*$  mesons are  $J^P \in \{0^-, 1^-\}$ . In terms of  $SU(2)$  irreducible representations  $J^P = 0^-$  corresponds to a singlet  $\mathbf{1} \in I(SU(2))$  and  $J^P = 1^-$  to a triplet  $\mathbf{3} \in I(SU(2))$ . The result of the decomposition defined in equation (2.21) is a doublet  $\mathbf{2}$  with  $S = 0$ , three channels with  $S = 1$  each having dimension  $\mathbf{3}$  and a single-channel with  $S = 2$  and dimension  $\mathbf{5}$ . To decompose equation (2.15) with respect to total spin  $S \in \{0, 1, 2\}$ , the Clebsch-Gordan coefficients that make the decomposition into irreducible representations with associated meson content explicit must be computed. Equation (2.15) can then be transformed into the form

$$\tilde{H}\vec{\psi}_S = (CHC^{-1})(C\vec{\psi}_M) = E(C\vec{\psi}_M) = E\vec{\psi}_S, \quad (2.22)$$

where  $\vec{\psi}_S := C\vec{\psi}_M$  is a wave-function vector projected to definite total spin  $S$ ,  $C \in \mathbb{C}^{16 \times 16}$  is a transformation matrix whose entries are related to the Clebsch-Gordan coefficients, corresponding to the decomposition in equation (2.21) (for details see [63]) and  $\tilde{H} := CHC^{-1}$  is the transformed hamiltonian. With this transformation, equation (2.15) assumes the following block structure

$$\left[ \begin{array}{cccc} \tilde{H}_{S=0,2 \times 2} & 0 & 0 & 0 \\ 0 & \mathbb{1}_{3 \times 3} \otimes \tilde{H}_{S=1,1 \times 1} & 0 & 0 \\ 0 & 0 & \mathbb{1}_{3 \times 3} \otimes \tilde{H}_{S=1,2 \times 2} & 0 \\ 0 & 0 & 0 & \mathbb{1}_{5 \times 5} \otimes \tilde{H}_{S=2,1 \times 1} \end{array} \right] - E \left[ \begin{array}{c} \vec{\Psi}_{S=0,2 \times 2} \\ \vec{\Psi}_{S=1,3 \times 3} \\ \vec{\Psi}_{S=1,5 \times 5} \\ \vec{\Psi}_{S=2,8 \times 8} \end{array} \right] = 0 \quad (2.23)$$

with blocks

**S=0 :**

For  $S = 0$ , there is a  $2 \times 2$  coupled channel equation that contains a  $BB$  and a  $B^*B^*$  channel

$$\left[ \begin{pmatrix} 2m_B & 0 \\ 0 & 2m_{B^*} \end{pmatrix} - \frac{1}{2\mu} \left( \frac{\partial^2}{\partial r^2} + \frac{2}{r} \frac{\partial}{\partial r} - \frac{\mathbf{L}^2}{r^2} \right) \otimes \mathbb{1}_{2 \times 2} + H_{\text{int}, S=0} \right] \vec{\Psi}_{S=0}(\mathbf{r}) = E \vec{\Psi}_{S=0}(\mathbf{r}), \quad (2.24)$$

where

$$H_{\text{int}, S=0} = \frac{1}{4} \begin{pmatrix} V_5(r) + 3V_j(r) & \sqrt{3}(V_5(r) - V_j(r)) \\ \sqrt{3}(V_5(r) - V_j(r)) & 3V_5(r) + V_j(r) \end{pmatrix} \quad (2.25)$$

is the  $2 \times 2$  potential matrix.

The 2-component wave function  $\vec{\Psi}_{S=0}$  can be related to  $B$  and  $B^*$  channels as

$$\vec{\Psi}_{S=0} = \begin{pmatrix} BB \\ \frac{\vec{B}^* \vec{B}^*}{\sqrt{3}} \end{pmatrix}. \quad (2.26)$$

Note that for  $S = 0$  no  $BB^*$  combinations appear because this combination can only have  $S = 1$ . Conversely,  $BB$  combinations can only have total spin  $S = 0$  and  $B^*B^*$  combinations can have total spin  $S \in \{0, 1, 2\}$ .

### S=1:

For  $S = 1$  a threefold degeneracy of  $k := S_z \in \{-1, 0, 1\}$  is present. The governing  $3 \times 3$  block can be further split by symmetrizing/antisymmetrizing the  $BB^*$  wave functions. For a wave function that is symmetric under  $B/B^*$  exchange there are three degenerate  $1 \times 1$  equations

$$\left[ m_B + m_{B^*} - \frac{1}{2\mu} \left( \frac{\partial^2}{\partial r^2} + \frac{2}{r} \frac{\partial}{\partial r} - \frac{\mathbf{L}^2}{r^2} \right) + H_{\text{int}, S=1, 1 \times 1} \right] \Psi_{S=1, 1 \times 1, k}(\vec{r}) = E \psi_{S=1, 1 \times 1, k}(\mathbf{r}) \quad (2.27)$$

with

$$H_{\text{int}, S=1, 1 \times 1} = V_j(r), \quad \Psi_{S=1, 1 \times 1, k} = \frac{1}{\sqrt{2}} (BB_k^* + B_k^*B) \quad (2.28)$$

For a wave function that is antisymmetric under  $B/B^*$  exchange, there are three degenerate  $2 \times 2$  equations.

$$\left[ \begin{pmatrix} m_B + m_{B^*} & 0 \\ 0 & 2m_{B^*} \end{pmatrix} - \frac{1}{2\mu} \left( \frac{\partial^2}{\partial r^2} + \frac{2}{r} \frac{\partial}{\partial r} - \frac{\mathbf{L}^2}{r^2} \right) \otimes \mathbb{1}_{2 \times 2} + H_{\text{int}, S=1, 2 \times 2} \right] \vec{\Psi}_{S=1, 2 \times 2, k}(\mathbf{r}) = E \vec{\Psi}_{S=1, 2 \times 2, k}(\mathbf{r}), \quad (2.29)$$

where

$$H_{\text{int}, S=1, 2 \times 2} = \frac{1}{2} \begin{pmatrix} V_5(r) + V_j(r) & V_5(r) - V_j(r) \\ V_5(r) - V_j(r) & V_5(r) + V_j(r) \end{pmatrix}, \quad \vec{\Psi}_{S=1, 2 \times 2, k} = \frac{1}{\sqrt{2}} \begin{pmatrix} B_k^*B - BB_k^* \\ \epsilon_{klm} B_l^* B_m^* \end{pmatrix} \quad (2.30)$$

### S=2:

For  $S = 2$  there is a five-fold degeneracy of  $k := S_z \in \{2, -1, 0, 1, 2\}$ . There are five identical single-channel equations which contain only  $B^*B^*$  combinations.

$$\left[ 2m_{B^*} - \frac{1}{2\mu} \left( \frac{\partial^2}{\partial r^2} + \frac{2}{r} \frac{\partial}{\partial r} - \frac{\mathbf{L}^2}{r^2} \right) + H_{\text{int}, S=2} \right] \Psi_{S=2, k}(\vec{r}) = E \Psi_{S=2, k}(\vec{r}), \quad (2.31)$$

where

$$H_{\text{int}, S=2} = V_j(r), \quad \Psi_{S=2, k} = T_{2, k}(\vec{B}^*, \vec{B}^*) \quad (2.32)$$

with  $T_{2, k}(\vec{B}^*, \vec{B}^*)$  being a spherical tensor which represents the coupling of two  $B^*$  mesons to  $S = 2$ .

The physical interpretation of equations (2.24)-(2.31) becomes apparent, once proper physical quantum numbers  $I(J^P)$  are assigned. This will be addressed in detail in section 2.5.



## 2.5 Symmetries and Quantum Numbers

A four-quark system is characterized by the following conserved quantum numbers:

- Isospin  $I$
- Total angular momentum, parity and charge conjugation  $J^{PC}$

At the beginning of section 2.4 I argued that the total spin  $S$  and the orbital angular momentum  $L$  are also conserved quantum numbers of the system. Each conserved quantum number is a consequence of a symmetry, described by a symmetry group. For instance, the total spin  $S$  is described by the group  $SU(2)_{\text{spin}}$ . Light quark flavor is described by the group  $SU(2)_{\text{flavor}}$ , color combination by the group  $SU(3)_{\text{color}}$ , orbital angular momentum by the group  $SO(3)_L$  and parity by the discrete group  $\mathbb{Z}_{2,\text{parity}}$ . The total symmetry group of the  $\bar{b}b\bar{u}d$  four-quark system corresponds to the product group

$$SU(2)_{\text{spin}} \times SU(2)_{\text{flavor}} \times SU(3)_{\text{color}} \times (\mathbb{Z}_{2,\text{parity}} \rtimes SO(3)_L), \quad (2.33)$$

where  $\rtimes$  denotes the semidirect product between  $\mathbb{Z}_{2,\text{parity}}$  and  $SO(3)_L$ . Quantum numbers of individual quarks can be grouped into irreducible representations of the underlying symmetry groups. Quantum numbers of the entire system are derived by combinations of quantum numbers of its composites. Products of two irreducible representations can be either symmetric(S) or antisymmetric(A). Since quarks are fermions, thus have to obey the Pauli principle, the total light-quark wave-function  $qq$  and heavy-quark wave function  $\bar{Q}\bar{Q}$  must be totally antisymmetric respectively. This means, only antisymmetric combinations of irreducible representations are allowed. In **Table 2.1** all possible combinations of individual quark quantum numbers, respecting the Pauli principle are shown. The parity  $P \in \{+, -\}$  is determined by the orbital angular momentum  $L$  according to

$$P = (-1)^L. \quad (2.34)$$

Subsequently, for  $P = -$  states only odd orbital angular momenta  $L$  are allowed, whereas for  $P = +$  states only even orbital angular momenta are allowed. Here, the discussion is restricted to odd orbital angular momenta  $L$  since this work focuses on the negative parity state  $I(J^P) = 0(1^-)$ . For a similar discussion for even orbital angular momenta  $L$  and an equivalent table as **Table 2.1**, I refer to [63].

combination	light quarks $qq$			heavy quarks $\bar{Q}\bar{Q}$			tetraquark $\bar{b}b\bar{u}d$	
	isospin	spin	color	spin	color	L	S	$J^P$
1	$1(S)$	$0(A)$	$6(S)$	$1(S)$	$\bar{6}(S)$	$1, 3, \dots(A)$	1	$ 1 - L ^- \leq J^- \leq  1 + L ^-$
2		$1(S)$	$\bar{3}(A)$	$0(A)$	$3(A)$		1	
3	$0(A)$	$0(A)$	$\bar{3}(A)$	$0(A)$	$3(A)$	$1, 3, \dots(A)$	0	$L^-$
4		$1(S)$	$6(S)$	$1(S)$	$\bar{6}(S)$		0,1,2	$ S - L ^- \leq J^- \leq  S + L ^-$

**Table 2.1:** Quantum numbers for  $\bar{b}b\bar{u}d$  states with odd orbital angular momenta  $L$

**Table 2.1** contains 4 combinations with different quantum numbers. Each of these combinations can be related to the blocks of definite total spin  $S \in \{0, 1, 2\}$ , defined in equations (2.24)-(2.31) via the Fierz identity (2.9) for a suitable combination of light quarks flavors for fixed isospin  $I$ .

Combinations 1 and 2 in **Table 2.1** are symmetric isotriplets with  $I = 1$ . The total light quark spin is  $S_q = 0$  for combination 1 and  $S_q = 1$  for combination 2. The color representation of the light quarks is fixed by enforcing the Pauli principle. In combination 1 the isospin wave function is symmetric and the light quark spin wave function is antisymmetric. To obtain an antisymmetric total wave function, the light quarks must be in a symmetric color sextet **6**. Conversely, in combination 2 the light quark spin wave function is symmetric, which requires the light quarks to be in an antisymmetric color triplet  **$\bar{3}$** .

The color combination of the light quarks determines the color combination of the heavy quarks. Because of gauge invariance, the total state must be color neutral. In terms of  $SU(3)$  irreducible representations this



means that the total decomposition of the product of two irreducible representations into irreducible representations is required to contain at least one singlet  $\mathbf{1} \in I(SU(3))$ . Following this logic, the color combination of the heavy quarks in combination 1 is fixed to the symmetric  $\bar{\mathbf{6}}$ , while the heavy quark color combination in combination 2 is fixed to the antisymmetric  $\mathbf{3}$ . The  $\bar{b}b$  wave function is always flavor symmetric. The orbital angular momentum  $L$  is odd, corresponding to an antisymmetric position wave function. The total heavy quark spin  $S_Q$  is fixed by enforcing the Pauli principle on the  $\bar{b}b$  wave function. This requirement leads to  $S_Q = 1$  for combination 1 and  $S_Q = 0$  for combination 2. This in turn leads to total spins of  $S = 1$  for both combinations. Correspondingly, the allowed total angular momenta are  $J \in [|1 - L|; 1 + L]$ . In terms of meson-meson pairs a total spin of  $S = 1$  can be realized by  $BB^*$  or  $B^*B^*$  combinations. Using Fierz identities, one finds that combinations 1 and 2 are associated with the  $S = 1$  block (2.29).

Combinations 3 and 4 in **Table 2.1** are antisymmetric isosinglets with  $I = 0$ . The total light quark spin can be either  $S_q = 0$  as in combination 3 or  $S_q = 1$  as in combination 4. The color representation of the light quarks is again uniquely fixed by enforcing the Pauli principle. In combination 3 both, the isospin wave function and the light quark spin wave functions are antisymmetric. To obtain an antisymmetric total wave function, the light quarks must be in an antisymmetric color triplet  $\bar{\mathbf{3}}$ . Conversely, in combination 2 the light quark spin wave function is symmetric, which requires the light quarks to be in a symmetric color sextet  $\mathbf{6}$ . By demanding color neutrality of the total state, the color combination of the heavy quarks in combination 3 is fixed to the antisymmetric  $\mathbf{3}$ , while the heavy quark color combination in combination 4 is fixed to the symmetric  $\bar{\mathbf{6}}$ . The orbital angular momentum  $L$  is odd, corresponding to an antisymmetric position wave function. The total heavy quark spin  $S_Q$  is again fixed by enforcing the Pauli principle on the  $\bar{b}b$  wave function, leading to  $S_Q = 0$  for combination 3 and  $S_Q = 1$  for combination 4. This in turn leads to a total spin of  $S = 0$  for combination 3 and total spin  $S \in \{0, 1, 2\}$  for combination 4. Correspondingly, the allowed total angular momenta for combination 3 are  $J = L$ . The allowed total angular momenta for combination 4 range over  $J \in [|S - L|; S + L]$ . In terms of meson-meson pairs a total spin of  $S = 0$  can be realized by  $BB$  or  $B^*B^*$  combinations, a total spin of  $S = 1$  can be realized by  $BB^*$  and  $B^*B^*$  combinations, and a total spin of  $S = 2$  can solely be realized by a  $B^*B^*$  combination. As the first two combinations of **Table 2.1** combinations 3 and combinations 4 can also be associated with blocks of definite  $S$ . Using the same procedure as for combinations 1 and 2 one finds that combination 3 can be associated to the  $S = 0$  block (2.24). Combination 4 on the other hand can be associated to each of the blocks defined in equations (2.24), (2.27) and (2.31).

In principle, all three block equations associated with combinations 3 and 4 describe a system with quantum numbers  $I(J^P) = 0(1^-)$ . However, not all of these blocks can actually describe resonance states. Resonances form only, when the potential is sufficiently attractive. The  $S = 0$  equation (2.24) has a distinguished potential matrix (2.25) from equations (2.27) and (2.31). Equations (2.27) and (2.31) contain only the repulsive potential  $V_j$  and no contribution from the attractive potential  $V_5$ . With such a potential no resonance will ever form. Equation (2.24) on the other hand contains  $V_5$  and  $V_j$ . Both potentials mix in the potential matrix (2.25). This does not a priori exclude the formation of a resonance or a bound state. Thus, equation (2.24) is the only viable candidate to describe the state of interest. This  $2 \times 2$  equation contains a  $BB$  and a  $B^*B^*$  combination and has  $S = 0$ .

### Single-channel limit for $S = 0$

In this short paragraph, I show that the single channel equation used in [64, 65] is a limiting case of equation (2.24). In the approach presented in this section heavy spin effects were introduced exclusively through the mass splitting  $m_{B^*} - m_B \neq 0$ . One would therefore assume that heavy spin effects are removed simply by setting  $m_B = m_{B^*}$ . In this limit  $B$  and  $B^*$  mesons are degenerate and the two equations in the  $2 \times 2$  block equation (2.24) should trivially decouple. Mathematically, this decoupling is equivalent to diagonalizing the full Hamiltonian. The only term of the full Hamiltonian which is not diagonal by design is the potential matrix (2.25). The potential matrix (2.25) can be diagonalized by the transformation

$$\begin{pmatrix} V_5 & 0 \\ 0 & V_j \end{pmatrix} = U H_{\text{int}, S=0} U^{-1}, \quad U = \begin{pmatrix} \frac{1}{2} & \frac{\sqrt{3}}{2} \\ -\frac{\sqrt{3}}{2} & \frac{1}{2} \end{pmatrix}. \quad (2.35)$$

Applying the same transformation to the mass matrix  $M = \text{diag}(2m_B, 2m_{B^*})$  yields the transformed mass matrix  $M'$

$$M' = U M U^{-1} = \frac{1}{2} \begin{pmatrix} m_B + 3m_{B^*} & \sqrt{3}(m_{B^*} - m_B) \\ \sqrt{3}(m_{B^*} - m_B) & 3m_B + m_{B^*} \end{pmatrix}. \quad (2.36)$$

In the degenerate mass limit, where  $m_B = m_{B^*}$ , the off-diagonal components of  $M'$  vanish and  $M' = M$ . In this limit equation (2.24) with the diagonalized Hamiltonian decouples into two independent single-channel equations

$$\left[ \begin{pmatrix} 2m_B & 0 \\ 0 & 2m_B \end{pmatrix} - \frac{\nabla^2}{2\mu} \otimes \mathbb{1}_{2 \times 2} + \begin{pmatrix} V_5 & 0 \\ 0 & V_j \end{pmatrix} \right] \vec{\Psi}_{S=0}(\mathbf{r}) = E \vec{\Psi}_{S=0}(\mathbf{r}). \quad (2.37)$$

The upper row of equation (2.37) corresponds precisely to the single-channel equation used in [64, 65] to study the  $I(J^P) = 0(1^-)$  resonance. This completes the proof presented in this paragraph and the discussion of the entire section.

## Chapter 3

# Coupled-Channel Scattering

In chapter 2 I concluded that the channel with total heavy spin  $S = 0$  is the most promising one for the study of a tetraquark resonance with quantum numbers  $I(J^P) = 0(1^-)$ . The corresponding equation which belongs to this channel is a  $2 \times 2$  coupled-channel equation. This differs compared to the case without heavy spins, explored in [64, 65], where it was sufficient to consider only a single-channel equation. To explore the impact of heavy spin effects for energies above the  $BB$  threshold, a refined  $2 \times 2$  scattering formalism is needed. For energies  $E > 2m_B$  the system is described by two scattering channels, one  $BB$  and one  $B^*B^*$  channel.

### 3.1 Emergent Wave Method

In the  $2 \times 2$  scattering problem with a  $BB$  and a  $B^*B^*$  channel, each channel is characterized by its channel momentum  $k_\alpha, \alpha \in \{BB, B^*B^*\}$  which is related to the energy  $E$  by the non-relativistic dispersion relation

$$k_{BB} = \sqrt{2\mu(E - 2m_B)}, \quad k_{B^*B^*} = \sqrt{2\mu(E - 2m_{B^*})}. \quad (3.1)$$

In the remainder of this work, I use the shorthand notation  $k := k_{BB}$  and  $k^* := k_{B^*B^*}$ .

Following the emergent wave method in [12, 54, 67], the wave function of the scattering problem is decomposed into two parts, namely into an incoming wave  $\vec{\psi}_0$  and an outgoing emergent wave for each of the two channels  $BB$  and  $B^*B^*$ . The total two-component wave function  $\vec{\Psi}(\vec{r})$  can be written as a sum of the incoming wave  $\vec{\Psi}_0(\vec{r})$  and the emergent spherical wave  $\vec{X}(\vec{r})$

$$\vec{\Psi}(\vec{r}) = \vec{\Psi}_0(\vec{r}) + \vec{X}(\vec{r}). \quad (3.2)$$

For a scattering process in a spherical symmetric potential  $V(r)$ , where  $\mathbf{L}$  is conserved, for  $S = 0$  the eigenfunctions of  $\mathbf{J}^2$  are equivalent to the eigenfunctions of  $\mathbf{L}^2$ . The latter are the well known spherical harmonics  $Y_{L,m}(\theta, \phi)$ , with azimuthal quantum number  $m \in [-L; L]$ . The total wave function defined in equation (3.2) can be expanded in an infinite sum of partial waves with fixed  $L$ . Different expansions are used for the incoming and the outgoing waves. The expansion for the incoming wave  $\vec{\Psi}_0$  reads

$$\vec{\Psi}_0(\vec{r}) = \sum_{L=0}^{\infty} c_L \vec{A}_L j_L(kr) Y_{L,m}(\theta, \phi), \quad (3.3)$$

where  $\vec{A}_L = (A_{BB}, A_{B^*B^*})^T$  is a vector of free coefficients that fixes the channel composition of the incoming wave,  $c_L = i^l \sqrt{4\pi(2L+1)}$  are well known expansion coefficients and  $j_L(kr)$  are spherical Bessel functions of first kind.

The emergent wave function  $\vec{X}(\vec{r})$  may be expanded in terms of angular momentum eigenfunctions as

$$X_\alpha(\vec{r}) = \sum_L c_L \frac{\chi_{L,\alpha}(r)}{r} Y_{L,m}(\theta, \phi), \quad (3.4)$$

where  $\alpha \in \{BB, B^*B^*\}$  refers to the channel composition and  $\chi_{L,\alpha}(r)$  denotes the  $L$ th partial wave of the radial part of the emergent wave. Hence, the total wave function can be expressed according to

$$\vec{\Psi}(\vec{r}) = \sum_{L=0}^{\infty} c_L \begin{pmatrix} A_{BB} j_L(kr) + \frac{\chi_{BB}(r)}{r} \\ A_{B^*B^*} j_L(k^*r) + \frac{\chi_{B^*B^*}(r)}{r} \end{pmatrix} Y_{L,m}(\theta, \phi). \quad (3.5)$$

The right hand side of equation (3.5) is an infinite sum over orbital angular momenta  $L \in \mathbb{N}$ . In practice, however the sum is truncated by a maximal orbital angular momentum  $L_{\max}$ . In this work, only  $p$ -wave scattering ( $L = 1$ ) is considered, leading to the right quantum numbers  $J^P = 1^-$ . After inserting equation (3.5) into (2.24), one can project to definite  $L = 1$  by multiplying the equation with  $Y_{1,m'}(\Omega)$  and integrating the equation over the unit area. By using the orthonormality of the spherical harmonics, the remaining radial equation becomes

$$\bullet \int d\Omega Y_{1,m'}(\Omega) \times (2.24) :$$

$$\left[ \begin{pmatrix} 2m_B & 0 \\ 0 & 2m_{B^*} \end{pmatrix} - \frac{1}{2\mu} \left( \frac{d^2}{dr^2} + \frac{2}{r} \frac{d}{dr} - \frac{2}{r^2} \right) \otimes \mathbb{1}_{2 \times 2} + H_{\text{int}, 2 \times 2} - E \right] \begin{pmatrix} A_{BB} j_1(kr) + \frac{\chi_{BB}(r)}{r} \\ A_{B^*B^*} j_1(k^*r) + \frac{\chi_{B^*B^*}(r)}{r} \end{pmatrix} = 0 \quad (3.6)$$

with potential matrix  $H_{\text{int}, 2 \times 2}$  defined in (2.25).

Equation (3.6) can be further manipulated by using the free Schroedinger equation  $H_0 \vec{\Psi}_0(\vec{r}) = E \vec{\Psi}_0(\vec{r})$ . Let  $H := H_0 + H_{\text{int}}$  be the total Hamiltonian with  $H_0 \vec{\Psi}_0 = E \vec{\Psi}_0$  then

$$\begin{aligned} (H - E) \vec{\Psi}(\vec{r}) &= (H_0 + H_{\text{int}} - E) (\vec{\Psi}_0(r) + \vec{X}(r)) = (H_0 - E) \vec{\Psi}_0(r) + H_{\text{int}} \vec{\Psi}_0(r) \\ &\quad + (H_0 + H_{\text{int}} - E) \vec{X}(r) \\ &= (H_0 + H_{\text{int}} - E) \vec{X}(r) + H_{\text{int}} \vec{\Psi}_0(r) = 0. \end{aligned} \quad (3.7)$$

In terms of a matrix vector notation this leads to the modified radial equation

$$\begin{aligned} &\left[ \begin{pmatrix} 2m_B & 0 \\ 0 & 2m_{B^*} \end{pmatrix} - \frac{1}{2\mu} \left( \frac{d^2}{dr^2} - \frac{2}{r^2} \right) \otimes \mathbb{1}_{2 \times 2} + H_{\text{int}, 2 \times 2} - E \right] \begin{pmatrix} \chi_{BB}(r) \\ \chi_{B^*B^*}(r) \end{pmatrix} \\ &= - \begin{pmatrix} \left( \frac{V_5 + 3V_j}{4} \right) r A_{BB} j_1(kr) + \frac{\sqrt{3}}{4} (V_5 - V_j) r A_{B^*B^*} j_1(k^*r) \\ \frac{\sqrt{3}}{4} (V_5 - V_j) r A_{BB} j_1(kr) + \left( \frac{3V_5 + V_j}{4} \right) r A_{B^*B^*} j_1(k^*r) \end{pmatrix}. \end{aligned} \quad (3.8)$$

Equation (3.8) is a system of two second order, inhomogenous ordinary differential equations. The inhomogenous part of equation (3.8) is fully dictated by the set of coefficients  $(A_{BB}, A_{B^*B^*})$ . In section 3.2 the freedom in fixing these coefficients will be used to define suitable boundary conditions.

For a specific energy range, it is often beneficial to use the energy relative to the lowest energy threshold  $E_{\text{th}} \in \mathbb{R}$ . For the scattering problem studied in this section the lowest energy threshold is the  $BB$  threshold, i.e.  $E_{\text{th}} = 2m_B$ . Defining  $\tilde{E} := E - 2m_B$  and rewriting equation (3.8) in terms of this new quantity, gives the following reformulated equation

$$\begin{aligned} &\left[ \begin{pmatrix} 0 & 0 \\ 0 & 2\Delta m \end{pmatrix} - \frac{1}{2\mu} \left( \frac{d^2}{dr^2} - \frac{2}{r^2} \right) \otimes \mathbb{1}_{2 \times 2} + H_{\text{int}, 2 \times 2} - \tilde{E} \right] \begin{pmatrix} \chi_{BB}(r) \\ \chi_{B^*B^*}(r) \end{pmatrix} \\ &= - \begin{pmatrix} \left( \frac{V_5 + 3V_j}{4} \right) r A_{BB} j_1(kr) + \frac{\sqrt{3}}{4} (V_5 - V_j) r A_{B^*B^*} j_1(k^*r) \\ \frac{\sqrt{3}}{4} (V_5 - V_j) r A_{BB} j_1(kr) + \left( \frac{3V_5 + V_j}{4} \right) r A_{B^*B^*} j_1(k^*r) \end{pmatrix}, \end{aligned} \quad (3.9)$$

where  $\Delta m = m_{B^*} - m_B$  is the mass splitting. Equation (3.9) as it stands has an infinite amount of possible solutions. To reduce the space of solution to a single physically relevant solution, consistent boundary conditions are needed. This is addressed in detail in section 3.2.

### Inelastic thresholds and light meson exchange

In addition to the  $BB$  and a  $B^*B^*$  channels also the inelastic three-particle channels  $BB\pi$  and  $B^*B^*\pi$ , where  $\pi$  describes a pion may contribute. The  $BB\pi$  threshold is only 50 MeV above the  $B^*B^*$  threshold and the  $B^*B^*\pi$  threshold is 140 MeV above the  $B^*B^*$  threshold for physical pion mass  $m_\pi \approx 140$  MeV. These inelastic channels introduce a mixing between two- and three-particle scattering channels.

The Born-Oppenheimer approximation is intrinsically designed to allow only for elastic scattering. In non-relativistic quantum mechanics particle production and/or annihilation is not allowed. This prohibits mixing between a scattering channel with an even number of particles and a scattering channel with an odd number of particles. The Born-Oppenheimer approximation is also limited by the static approximation to explicit non-relativistic degrees of freedom. Light degrees of freedom like the pion are integrated out by the static approximation and only contribute through the static potentials. This allows only for scattering channels which consist of heavy mesons. Pion exchange between the heavy mesons should in principle be contained in the static potentials  $V_5$  and  $V_j$ . Because the assumptions of the Born-Oppenheimer approximation prohibit mixing between two- and three-particle channels and integrate out the pion as a light degree of freedom, the inelastic scattering channels  $BB\pi$  and  $B^*B^*\pi$  cannot be included into the formalism presented in this section. This limits the approach of this work to resonances which are significantly below the first three particle threshold, where three-particle effects are expected to be negligible. For systems where the energy gap between two-particle and three-particle thresholds is small, the approach shouldn't be used as it does not incorporate all of the relevant physics. This limitation should be kept in mind, whenever the Born-Oppenheimer approximation is used.

## 3.2 Boundary Conditions and T Matrix

Suitable boundary conditions for small  $r \rightarrow 0$  and large  $r \rightarrow \infty$  are required to find a unique solution of the Schroedinger equation (3.9) in order to calculate observables such as the scattering amplitude or the cross section. Similarly to the case in [70], I use modified scattering boundary conditions for sufficiently large distances  $r$ . For a single-channel scattering problem in a spherically symmetric potential with given orbital angular momentum  $L$ , the boundary conditions for the spherical wave function read

$$\chi(r) \rightarrow irt_L h_L(kr), \quad r \rightarrow \infty \quad (3.10)$$

$$\chi(r) \propto r^{L+1}, \quad r \rightarrow 0, \quad (3.11)$$

where  $t_L \in \mathbb{C}$  is the single channel partial wave scattering amplitude and  $h_L(kr)$  are the spherical hankel functions of first kind.

For a two channel scattering problem the scattering boundary conditions must be employed on each wave function component  $\chi_\alpha(r)$ . Thereby, one can make use of the freedom choice for the incident wave composition by solving the equation independently for the pairs  $(A_{BB}, A_{B^*B^*}) = (1, 0)$  and  $(A_{BB}, A_{B^*B^*}) = (0, 1)$ . Following this procedure, boundary conditions for large radial distances  $r$  can be defined as

**For**  $(A_{BB}, A_{B^*B^*}) = (1, 0)$  :

$$\begin{aligned} \chi_{BB}(r) &\rightarrow irt_{BB;BB} h_1(kr) & r \rightarrow \infty \\ \chi_{B^*B^*}(r) &\rightarrow irt_{B^*B^*;BB} h_1(k^*r) & r \rightarrow \infty \end{aligned} \quad (3.12)$$

**For**  $(A_{BB}, A_{B^*B^*}) = (0, 1)$  :

$$\begin{aligned} \chi_{BB}(r) &\rightarrow irt_{BB;B^*B^*} h_1(kr) & r \rightarrow \infty \\ \chi_{B^*B^*}(r) &\rightarrow irt_{B^*B^*;B^*B^*} h_1(k^*r) & r \rightarrow \infty \end{aligned} \quad (3.13)$$

with a priori unknown scattering amplitudes  $t_{\alpha;\beta} \in \mathbb{C}$ , where  $\alpha \in \{BB, B^*B^*\}$  refers to the incoming wave and  $\beta \in \{BB, B^*B^*\}$  refers to the outgoing emergent wave. Boundary conditions for  $r \rightarrow 0$  are identical to

the ones used in [65], i.e. for  $L = 1$

$$\chi_{BB}(r) \propto r^2, \quad r \rightarrow 0 \quad (3.14)$$

$$\chi_{B^*B^*}(r) \propto r^2, \quad r \rightarrow 0. \quad (3.15)$$

The four scattering amplitudes  $t_{\alpha;\beta}$  can be extracted a posteriori from the boundary conditions (3.12)-(3.13), fixing the entries of the  $2 \times 2$  T matrix

$$\mathbf{T} = \begin{pmatrix} t_{BB;BB} & t_{BB;B^*B^*} \\ t_{B^*B^*;BB} & t_{B^*B^*;B^*B^*} \end{pmatrix}. \quad (3.16)$$

The T matrix defined in equation (3.16) depends on the energy  $E$  and can be used to detect bound states or resonances. Poles of the T matrix in the complex energy plane  $E \in \mathbb{C}$  indicate resonances for  $\text{Re}(\tilde{E}) > 0$  and  $\text{Im}(\tilde{E}) \neq 0$  or bound states for  $\text{Re}(\tilde{E}) < 0$  and  $\text{Im}(\tilde{E}) = 0$ . Resonance poles can be extracted by analytically continuing the T matrix to unphysical Riemann sheets as explained in detail in section 3.4. Poles of the T matrix are equivalent to poles of its eigenvalues which in turn is equivalent to poles of the T matrix determinant  $\det(\mathbf{T})$ . In all numerical calculations of this work the determinant is used to detect poles. If a pole is found at energy  $E_{\text{pole}}$ , then the corresponding mass  $m := \text{Re}(\tilde{E}_{\text{pole}}) + 2m_B$  and the corresponding width  $\Gamma := -2\text{Im}(\tilde{E}_{\text{pole}})$ <sup>1</sup> can be extracted. The pair  $(m, \Gamma)$  categorises all resonances and can be compared to experimental data if available.

This section is concluded with a short remark on scattering phase shifts. The T matrix defined in equation (3.16) is related to the unitary S matrix  $\mathbf{S} \in U(2)$  as

$$\mathbf{S} = 1 + 2i\mathbf{T}. \quad (3.17)$$

The unitarity condition of the S matrix  $\mathbf{S}^\dagger \mathbf{S} = 1$  allows one to express the S matrix for the single-channel case i.e.  $\mathbf{S} \in U(1)$  in terms of a real partial wave phase shift  $\delta_l(E) \in \mathbb{R}$

$$\mathbf{S} = e^{2i\delta_l(E)}. \quad (3.18)$$

The definition of a phase shift for the two channel case is far less obvious and more involved. In general this requires the concept of eigenphases and can be accomplished by using the S matrix eigenvalues as presented in the following section 3.3.

### 3.3 Coupled-Channel Phase Shifts

A consistent definition of a coupled-channel phase shift is given in [70], where the concept of eigenphases is introduced. To each scattering channel a corresponding eigenphase can be assigned. For an  $n$ -channel scattering problem, eigenphases  $\delta_\alpha(E)$  with  $\alpha \in \{1, 2, \dots, n\}$  can be calculated by applying relation (3.18) to the S matrix eigenvalues  $s_\alpha(E) \in \mathbb{C}$  for real energies  $E \in \mathbb{R}$ :

$$s_\alpha(E) = e^{2i\delta_\alpha(E)}. \quad (3.19)$$

For  $n = 2$  the following analytic relations can be found for the two S matrix eigenvalues  $s_\alpha(E)$ ,  $\alpha \in \{1, 2\}$

$$s_1(E) = \frac{\xi}{2} + \sqrt{\frac{\xi^2}{4} - (s_{BB;BB}s_{B^*B^*;B^*B^*} - s_{BB;B^*B^*}s_{B^*B^*;BB})} \quad (3.20)$$

$$s_2(E) = \frac{\xi}{2} - \sqrt{\frac{\xi^2}{4} - (s_{BB;BB}s_{B^*B^*;B^*B^*} - s_{BB;B^*B^*}s_{B^*B^*;BB})}, \quad (3.21)$$

where  $s_{\alpha;\beta} = \delta_{\alpha\beta} + 2it_{\alpha;\beta}$  denote the entries of the S matrix and  $\xi := s_{BB;BB} + s_{B^*B^*;B^*B^*}$ . With equation (3.19) two phase shifts  $\delta_1(E), \delta_2(E)$  can be extracted. For given real energy  $E \in \mathbb{R}$  one of these phase shifts can be associated with the  $BB$  channel and one with the  $B^*B^*$  channel. Depending on the energy  $E$ ,  $\delta_\alpha(E)$  can now be either real or complex. For energies  $2m_B < E < 2m_{B^*}$  the phase shift which can be associated with the  $BB$  channel assumes real values while the phase shift associated with the  $B^*B^*$  channel is purely imaginary. For energies  $E > 2m_{B^*}$  both phase shifts assume real values. Strong signals of poles in the T

<sup>1</sup>These relations are derived by expanding T via a Breit-Wigner parametrization

matrix can be detected by a swift rise in the eigenphases  $\delta_\alpha(E)$  from 0 to  $\pi/2$ . Strictly speaking, this claim is accurate only for poles located in the vicinity of the real axis. For poles located close to the real axis the phase shifts can suit as a good indicator to detect resonances. For weak signals or poles that have large corresponding widths  $\Gamma$ , such a relation does not exist. For such cases the phase shifts is not a good indicator for the existence of a resonance.

### 3.4 Riemann Sheets and Analytical Structure

The notion of Riemann sheets is an important part of physical scattering problems. Mathematically, for a complex-valued function  $f : \mathbb{C} \rightarrow \mathbb{C}$  different Riemann sheets describe discontinuous regions in the complex plane and are separated by branch cuts. In a scattering problem such branch cuts are located along the real energy axis with branch points at threshold energies. Depending on which Riemann sheet a pole of the scattering amplitude is located, the physical interpretation of this pole changes.

#### 3.4.1 General Definition

For general double-valued complex functions  $f : D \rightarrow \mathbb{C}$  with  $D \subset \mathbb{C}$  the concept of Riemann sheets can be defined as follows

##### Definition 1: Riemann Sheets

Let  $D \in \mathbb{C}$  an let  $f : D \rightarrow \mathbb{C}$  be a double-valued complex function. Let further  $z_0, z_1 \in \mathbb{C}$  be two branch points of  $f$  which generate a branch cut  $\gamma : [z_0, z_1] \rightarrow \mathbb{C}$  with end points  $z_0$  and  $z_1$ , then two branches  $f_1 : R_1 \rightarrow \mathbb{C}$  and  $f_2 : R_2 \rightarrow \mathbb{C}$  separated by the branch cut can be defined. The domains  $R_1, R_2 \subset \mathbb{C}$  are called **Riemann sheets**

In essence, Riemann sheets are two disconnected subdomains of a complex domain which are separated by a branch cut. A simple example is the complex square root  $f : z \mapsto \sqrt{z}$  which is a double-valued complex functions. The complex square root has branch points at  $z = 0$  and  $z = \infty$ , generating a right hand cut along  $[0; \infty)$ . The branch cut is chosen along the positive real axis. This separates two branches  $f_1 = \{\text{Im}(\sqrt{z}) \geq 0\}$  and  $f_2 = \{\text{Im}(\sqrt{z}) < 0\}$ . The corresponding Riemann sheets are  $R_I := \{z \in \mathbb{C} : \text{Im}(\sqrt{z}) \geq 0\} \setminus [0; \infty)$  and  $R_{II} := \{z \in \mathbb{C} : \text{Im}(\sqrt{z}) < 0\}$ .

#### 3.4.2 Single-Channel

A single-channel scattering problem is characterized by its channel momentum  $k \in \mathbb{C}$ . According to equation (3.1) the momentum is related to the energy  $E \in \mathbb{C}$  by a square root. For a single channel only one threshold  $E_{\text{th}}$  is present. The channel momentum  $k$  has a branch point precisely at  $E_{\text{th}}$ . This generates a right hand branch cut along  $[E_{\text{th}}; \infty)$  in the energy  $E$ . This branch cut separates two Riemann sheets I and II, defined by

$$R_I := \{E \in \mathbb{C} : \text{Im}(k) \geq 0\} \setminus [E_{\text{th}}; \infty), \quad R_{II} := \{E \in \mathbb{C} : \text{Im}(k) < 0\}. \quad (3.22)$$

Technically only the half with  $\text{Re}(k) \geq 0$  of each Riemann sheet is physically relevant, since the real part of the momentum should either be positive or zero. The physically relevant domain corresponds to the upper half of sheet I and the lower half of sheet II. Henceforth, whenever I will refer to a Riemann sheet in a scattering problem, I will only refer to the part with  $\text{Re}(k) \geq 0$ .

#### Classification of poles

Poles of the scattering amplitude are parts of its singular structure. Poles can be located on different Riemann sheets. The location of the pole in the complex momentum plane is crucial for its physical interpretation. There are three types of poles which have their own special physical meaning. To simplify notation in the single channel case, where only a single threshold is present, I will hereafter refer to  $\tilde{E} := E - E_{\text{th}}$  as the energy relative to this threshold.

### Bound states

For large radial distances  $r \rightarrow \infty$  the radial emergent wave function  $\chi_L(r)$  behaves as

$$\chi_L(r) \propto (e^{2i\delta_L} - 1) e^{ikr}, \quad (3.23)$$

where  $\delta_L$  denotes the Lth-partial wave phase shift. On the real energy axis, where  $\tilde{E} \in \mathbb{R}$  is the energy relative to the threshold and  $\tilde{E} < 0$ , the channel momentum  $k$  is purely imaginary and can take two different values

$$k = \pm i\sqrt{-2\mu\tilde{E}}. \quad (3.24)$$

For  $\text{Im}(k) > 0$ , the wave function in equation (3.23) decays exponentially for large  $r$  which is the correct asymptotic behavior for a bound state. Hence, poles of the scattering amplitude  $T$  with  $\text{Im}(k) \geq 0$  on the real-energy axis are called bound states. These poles are always located on the physical Riemann sheet I.

### Virtual bound states

From a mathematical perspective it is equally reasonable to choose  $\text{Im}(k) < 0$ . For  $\text{Im}(k) < 0$ , the wave function in equation (3.23) increases exponentially for large  $r$ . Poles of the scattering amplitude  $T$  with  $\text{Im}(k) < 0$  on the real axis do not correspond to asymptotic states. Such poles are called virtual bound states. These poles are located on the unphysical Riemann Sheet II.

### Resonances

Resonances are poles of the scattering amplitude  $T$  with nonzero imaginary part  $\text{Im}(E) \neq 0$ . For  $E \in \mathbb{C}$  the channel momentum  $k \in \mathbb{C}$  contains a real and imaginary part and is defined as

$$k = \sqrt{2\mu\tilde{E}}. \quad (3.25)$$

For  $\text{Re}(k) \neq 0$ , one can not infer any information about the two Riemann sheets from equation (3.23). Instead, one has to directly examine the scattering amplitude  $T$ . For energies  $E$  in the vicinity of a pole,  $T$  can be parametrized with a Breit-Wigner parametrization ([134])

$$T = -\frac{\Gamma/2}{E - m \pm i\Gamma/2} \quad (3.26)$$

with resonance mass  $m$  and corresponding width  $\Gamma$ . The minus sign in the denominator of (3.26) is used for energies  $E$  on Riemann sheet I, while the plus sign is used for energies on Riemann sheet II. Poles of the scattering amplitude in equation (3.26) correspond to roots of the denominator. The roots of the denominator are

$$E = m \mp i\frac{\Gamma}{2}. \quad (3.27)$$

Moreover, the scattering amplitude  $T$  must obey the unitarity constraint

$$\text{Im}(T) = |T|^2 \quad (3.28)$$

which is derived from the unitarity condition for the S matrix (see section 3.2). A full derivation can be found in appendix C. After inserting equation (3.26) into (3.28) and performing simple algebraic steps, the unitarity condition translates into

$$\frac{\Gamma^2/4}{(E - m)^2 + \Gamma^2/4} = \pm \frac{\Gamma^2/4}{(E - m)^2 + \Gamma^2/4}. \quad (3.29)$$

For nonzero  $\Gamma$  equation (3.29) is only fulfilled, if the + sign is chosen. The corresponding poles have  $\text{Im}(E) < 0$  which is equivalent to  $\text{Im}(k) < 0$ . Physical resonances are thus always located on Riemann sheet II. Poles with  $\text{Im}(k) > 0$ , located on the first Riemann sheet are unphysical, because they violate the unitarity constraint (3.28). Such unphysical poles can still remotely contribute to calculations of experimental observables, for example the cross section, if their location is close enough to the real energy axis. The full sheet structure of the single channel physical scattering amplitude is depicted in **Figure 3.1**, taken from [135]



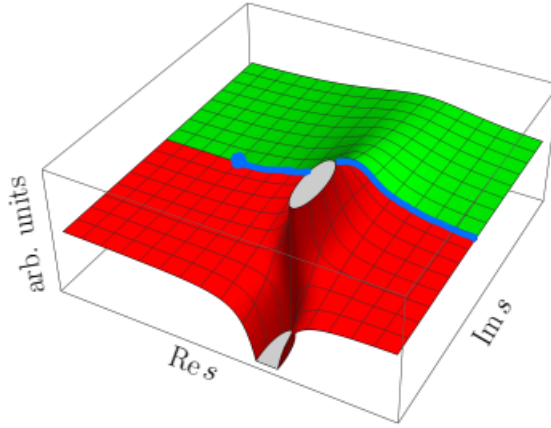


**Figure 3.1:** Analytical continuation of the scattering amplitude from the upper half plane of the first Riemann sheet with positive imaginary energy  $\text{Im}(s) > 0$  colored in green to the lower half plane of the second Riemann sheet with negative imaginary energy  $\text{Im}(s) < 0$  colored in red. The Riemann sheets are smoothly connected by the blue line which symbolizes the branch cut at  $\text{Im}(s) = 0$ . A physical pole of the scattering amplitude is depicted on the lower half plane of the second Riemann sheet

### 3.4.3 Two Channels

Two-channel scattering problems are more involved in their analytic structure than single-channel ones. In a two-channel scattering problem such as the  $\bar{b}bud$  system, studied in this work, there are two distinct thresholds  $E_{\text{th},\alpha}$ , resulting in two channel momenta  $k_\alpha$  with  $\alpha \in \{1, 2\}$ . Each momentum  $k_\alpha : \mathbb{C} \rightarrow \mathbb{C}$  can be thought of as a distinct complex-valued function which comes along with its own branch cut. The branch points of each channel momentum  $k_\alpha$  lies at the respective threshold  $E_{\text{th},\alpha}$ . Each branch point is accompanied by a right hand branch cut along  $[E_{\text{th},\alpha}; \infty)$ . Each branch cut separates two subdomains  $R_{\alpha,1}, R_{\alpha,2} \subset \mathbb{C}$  of the complex momentum plane, defined as

$$R_{\alpha,1} = \{E \in \mathbb{C} : \text{Im}(k_\alpha) \geq 0\} \setminus [E_{\text{th},\alpha}; \infty), \quad R_{\alpha,2} = \{E \in \mathbb{C} : \text{Im}(k_\alpha) < 0\}. \quad (3.30)$$

From these branches, four Riemann sheets can now be constructed from the intersection  $R_{ij} := R_{1,i} \cap R_{2,j}$  with  $i, j \in \{1, 2\}$ , defining a total of four Riemann sheets for the two channel scattering system. These Riemann sheets are ordered according to a classification scheme, taken from [74]

$$R_{ij} = \begin{cases} \text{I}, & \text{if } i = 1, j = 1 \\ \text{II}, & \text{if } i = 2, j = 1 \\ \text{III}, & \text{if } i = 2, j = 2 \\ \text{IV}, & \text{if } i = 1, j = 2 \end{cases}. \quad (3.31)$$

Other classification schemes are equally correct.

#### Classification of poles

As discussed in section 3.2, for two-channel scattering problems the scattering amplitude  $T$  becomes a  $2 \times 2$  matrix called  $T$  matrix. As in the single channel case, poles of the  $T$  matrix can be separated again into bound states, virtual bound states and resonances.

Poles with  $\text{Im}(E) = 0$  and  $\text{Re}(E) < E_{\text{th},1}$  are called bound states if and only if  $\text{Im}(k_1), \text{Im}(k_2) > 0$ , i.e. bound states are always located on Riemann sheet I. Poles with  $\text{Im}(E) = 0$  and  $\text{Re}(E) < E_{\text{th},1}$  on all other Riemann sheets entail a wrong asymptotic behavior in the wave function. Such poles are called virtual bound states. Poles off the real axis with  $\text{Im}(E) \neq 0$  are called resonances. The unitarity constraint (3.28) extended to coupled channels prohibits the existence of the resonance on Riemann sheet I. Correspondingly, resonances can appear on Riemann sheets II, III and IV.

The discussion in this paragraph also applies to the  $\bar{b}bud, I(J^P) = 0(1^-)$  system studied in this work. As

noted in section 3.2 the  $2 \times 2$  scattering problem consists of a  $BB$  scattering channel and  $B^*B^*$  scattering channel. The channel momenta defined in equation (3.1) have branch points at their respective thresholds at energies  $E = 2m_B$  for the  $BB$  and  $E = 2m_{B^*}$  for the  $B^*B^*$  channel. Poles with  $\text{Re}(E) < 2m_B$  and  $\text{Im}(E) = 0$  are identified as bound states, while poles away from the real axis with  $\text{Im}(E) < 0$  are identified as physical resonances if found on Riemann sheet III. Poles with  $\text{Re}(E) < 2m_B$  and  $\text{Im}(E) = 0$  found on Riemann sheets II, III or IV are identified as virtual bound states, while poles with  $\text{Im}(E) \neq 0$  found on Riemann sheets II or IV are identified as nonphysical resonances.

With this, the discussion of all facets of the theoretical scattering formalism, relevant for this work, is concluded. In the next section results from this section are used to develop a numerical method to study the  $\bar{b}b u d$ ,  $I(J^P) = 0(1^-)$  four quark channel with heavy spin effects.

### 3.5 Numerical Method

In this section, all preparatory steps needed before a numerical analysis is conducted are presented. The following paragraphs are meant as an overview about numerical preparations to bring equation (3.9) into a numerically solvable form, however I refrain from showing all intermediate algebraic steps. The techniques presented in this section are mostly equivalent to the ones used in following works [54, 67, 70].

In all numerical problems that involve physical quantities with units, the first step is to reformulate the equation, one is interested in solving in terms of dimensionless quantities, defined by a characteristic scale of the system, e.g. a mass or a length. For the system studied in this work a suitable choice is given by the lattice spacing  $a$ . After re-expressing all dimensionful quantities  $q$  in equation (3.9) through dimensionless quantities  $\hat{q}$ , the coupled ordinary differential equations (3.9) becomes

$$\begin{aligned} \frac{d^2}{d\hat{r}^2} \chi_{BB}(\hat{r}) &= \left[ \left( \frac{\hat{V}_5 + 3\hat{V}_j}{4} \right) \hat{r} A_{BB} j_1(\hat{k}\hat{r}) + \frac{\sqrt{3}}{4} (\hat{V}_5 - \hat{V}_j) \hat{r} A_{B^*B^*} j_1(\hat{k}^* \hat{r}) \right] \\ &+ \left[ \frac{\sqrt{3}}{4} (\hat{V}_5 - \hat{V}_j) \chi_{B^*B^*}(\hat{r}) + \left( \frac{2}{\hat{r}^2} + \frac{1}{4} (\hat{V}_5 + 3\hat{V}_j) - \hat{E} \right) \chi_{BB}(\hat{r}) \right] \end{aligned} \quad (3.32)$$

$$\begin{aligned} \frac{d^2}{d\hat{r}^2} \chi_{B^*B^*}(\hat{r}) &= \left[ \left( \frac{3\hat{V}_5 + \hat{V}_j}{4} \right) \hat{r} A_{B^*B^*} j_1(\hat{k}^* \hat{r}) + \frac{\sqrt{3}}{4} (\hat{V}_5 - \hat{V}_j) \hat{r} A_{BB} j_1(\hat{k}\hat{r}) \right] \\ &+ \left[ \frac{\sqrt{3}}{4} (\hat{V}_5 - \hat{V}_j) \chi_{BB}(\hat{r}) + \left( 2\Delta\hat{m} + \frac{2}{\hat{r}^2} + \frac{1}{4} (3\hat{V}_5 + \hat{V}_j) - \hat{E} \right) \chi_{B^*B^*}(\hat{r}) \right], \end{aligned} \quad (3.33)$$

where  $\hat{r} = r/a$  is a dimensionless radial coordinate. All precise, analytical relations between quantities  $q_i$  and their corresponding dimensionless equivalents  $\hat{q}_i$  are given in appendix A.

The system of differential equations above is a system of two coupled, linear, inhomogenous ordinary differential equation. The total solution of such a system is a combination of the solution of the homogenous equation and a solution of the total inhomogenous one. Let  $\vec{\chi}_{\text{hom}}^{(k)}(\hat{r}) := \left( \chi_{BB, \text{hom}}^{(k)}(\hat{r}), \chi_{B^*B^*, \text{hom}}^{(k)}(\hat{r}) \right)^T$  with  $k \in \{1, 2\}$  be two linearly independent solutions of the homogenous equation and  $\vec{\chi}_{\text{inh}}(\hat{r}) := \left( \chi_{BB, \text{inh}}(\hat{r}), \chi_{B^*B^*, \text{inh}}(\hat{r}) \right)^T$  one particular solution of the inhomogenous equation then the total solution  $\vec{\chi}_{\text{tot}}(\hat{r})$  reads

$$\vec{\chi}_{\text{tot}}(\hat{r}) = \vec{\chi}_{\text{inh}}(\hat{r}) + \alpha_1 \vec{\chi}_{\text{hom}}^{(1)}(\hat{r}) + \alpha_2 \vec{\chi}_{\text{hom}}^{(2)}(\hat{r}) \quad (3.34)$$

with two initially undetermined coefficients  $\alpha_1, \alpha_2 \in \mathbb{C}$ . The two solutions of the homogenous equation  $\vec{\chi}_{\text{hom}}^{(k)}(r)$  are determined by solving equation (3.9) with  $A_{BB} = A_{B^*B^*} = 0$ . In order to guarantee that the solutions are linearly independent, I choose the following initial conditions for the wave functions  $\vec{\chi}_{\text{hom}}^{(k)}(r)$

$$\vec{\chi}_{\text{hom}}^{(1)}(\hat{r}) \propto \begin{pmatrix} \hat{r}^2 \\ 0 \end{pmatrix}, \quad \vec{\chi}_{\text{hom}}^{(2)}(\hat{r}) \propto \begin{pmatrix} 0 \\ \hat{r}^2 \end{pmatrix}, \quad \hat{r} \rightarrow 0. \quad (3.35)$$

In the last step of the numerical method, the coefficients  $\alpha_1$  and  $\alpha_2$  need to be calculated. In the following paragraph, a general derivation of the coefficients  $\alpha_i \in \mathbb{C}$  with  $i \in \{1, 2\}$ , based on boundary conditions is outlined.

In numerical calculations the infinite radial distance  $r$  must be replaced by a sufficiently large maximum distance  $r_{\max}$  at which boundary conditions are satisfied up to a given numerical precision. To check for numerical stability the value of  $r_{\max}$  can be varied. The result of a numerical calculation should be largely independent of the concrete choice of  $r_{\max}$ .

The total wave function components  $\chi_{\alpha, \text{tot}}(r)$  with  $\alpha \in \{BB, B^*B^*\}$ , defined in (3.34) satisfies the boundary conditions defined in equations (3.12)-(3.13) for a fixed incident wave composition  $(A_{BB}, A_{B^*B^*})$ . By taking a logarithmic derivative of equation (3.12) or equation (3.13) at  $r = r_{\max}$ , one obtains a system of linear equations for the coefficients  $\alpha_1$  and  $\alpha_2$

$$\left. \frac{d}{dr} \log(\chi_{BB}(r)) \right|_{r=r_{\max}} = \frac{\chi'_{BB, \text{inh}}(r_{\max}) + \alpha_1 \chi'_{BB, \text{hom}}(r_{\max}) + \alpha_2 \chi'_{BB, \text{hom}}(r_{\max})}{\chi_{BB, \text{inh}}(r_{\max}) + \alpha_1 \chi_{BB, \text{hom}}(r_{\max}) + \alpha_2 \chi_{BB, \text{hom}}(r_{\max})} = \frac{r h_1'(kr) + h_1(kr)}{r h_1(kr)} \quad (3.36a)$$

$$\left. \frac{d}{dr} \log(\chi_{B^*B^*}(r)) \right|_{r=r_{\max}} = \frac{\chi'_{B^*B^*, \text{inh}}(r_{\max}) + \alpha_1 \chi'_{B^*B^*, \text{hom}}(r_{\max}) + \alpha_2 \chi'_{B^*B^*, \text{hom}}(r_{\max})}{\chi_{B^*B^*, \text{inh}}(r_{\max}) + \alpha_1 \chi_{B^*B^*, \text{hom}}(r_{\max}) + \alpha_2 \chi_{B^*B^*, \text{hom}}(r_{\max})}, \quad (3.36b)$$

$$= \frac{r h_1'(k^*r) + h_1(k^*r)}{r h_1(k^*r)}$$

where the primes imply derivatives with respect to  $r$ . Equations (3.36a) and (3.36b) can equivalently be written as a matrix-vector equation with solution vector  $\vec{\alpha} = \begin{pmatrix} \alpha_1 \\ \alpha_2 \end{pmatrix} \in \mathbb{C}^2$ :

$$\mathbf{M} \vec{\alpha} = \vec{C} \quad (3.37)$$

with matrix  $\mathbf{M} \in \mathbb{C}^{2 \times 2}$  and inhomogeneity vector  $\vec{C} \in \mathbb{C}^2$  defined as

$$\mathbf{M} = \begin{pmatrix} \chi_{BB, \text{hom}}^{(1),'}(r_{\max}) - \beta \chi_{BB, \text{hom}}^{(1)}(r_{\max}) & \chi_{BB, \text{hom}}^{(2),'}(r_{\max}) - \beta \chi_{BB, \text{hom}}^{(2)}(r_{\max}) \\ \chi_{B^*B^*, \text{hom}}^{(1),'}(r_{\max}) - \gamma \chi_{B^*B^*, \text{hom}}^{(1)}(r_{\max}) & \chi_{B^*B^*, \text{hom}}^{(2),'}(r_{\max}) - \gamma \chi_{B^*B^*, \text{hom}}^{(2)}(r_{\max}) \end{pmatrix} \quad (3.38a)$$

$$\vec{C} = \begin{pmatrix} \beta \chi_{BB, \text{inh}}(r_{\max}) - \chi'_{BB, \text{inh}}(r_{\max}) \\ \gamma \chi_{B^*B^*, \text{inh}}(r_{\max}) - \chi'_{B^*B^*, \text{inh}}(r_{\max}) \end{pmatrix} \quad (3.38b)$$

with intermediate quantities  $\beta \in \mathbb{C}$  and  $\gamma \in \mathbb{C}$ , given by

$$\beta = \frac{r h_1'(kr) + h_1(kr)}{r h_1(kr)} \quad (3.39)$$

$$\gamma = \frac{r h_1'(k^*r) + h_1(k^*r)}{r h_1(k^*r)} \quad (3.40)$$

For  $n$ -channel scattering problems equation (3.37) generalizes to a system of equations with  $n$  unknown coefficients  $\alpha_i, i \in \{1, 2, \dots, n\}$ . Formally, the solution of equation (3.37) can be written as  $\vec{\alpha} = \mathbf{M}^{-1} \vec{C}$ . Therefore, for an  $n$ -channel scattering problem, the determination of the solution vector  $\vec{\alpha}$  is equivalent to inverting an  $n \times n$  matrix. For the  $2 \times 2$  inverse of the matrix specified in equation (3.38a) there is a simple

analytical expression allowing for an analytical solution for  $\vec{\alpha}$ . The two resulting coefficient  $\alpha_1$  and  $\alpha_2$  read

$$\alpha_1 = \frac{M_{22}C_1 - M_{12}C_2}{M_{11}M_{22} - M_{12}M_{21}} \quad (3.41a)$$

$$\alpha_2 = \frac{M_{11}C_2 - M_{21}C_1}{M_{11}M_{22} - M_{12}M_{21}}. \quad (3.41b)$$

Note that in all numerical calculations  $r$  must be replaced by  $\hat{r}$  and  $k$  by  $\hat{k}$ . With the coefficients  $\alpha_i$  determined, the total wave function can now be computed through equation (3.34). From the coefficients  $\alpha_1$  and  $\alpha_2$  the total wave function defined in equation (3.34) can be computed which in turn can be used to extract the T matrix elements  $t_{\alpha,\beta}$  with the boundary conditions defined in section 3.2. With this, the discussion of all preparatory steps for the numerical analysis contained in this work is concluded.

## Chapter 4

# Numerical Results

In this section results of the numerical analysis for the two-channel scattering problem defined by equation (3.9) are presented. Thereby, methods developed in chapter 3 are applied to compute various quantities that characterize the  $\bar{b}bud, I(J^P) = 0(1^-)$  four-quark system considered in this work. Based on the results, I draw conclusions for physical implications of heavy spin effects on the particular system studied in this work.

### 4.1 Numerical Procedure and Error Analysis

#### 4.1.1 Numerical Procedure and Input Parameters

The  $2 \times 2$  coupled-channel ordinary differential equation (3.9) is solved for complex energies  $E \in \mathbb{C}$  with a standard fourth-order Runge-Kutta algorithm. By employing the boundary conditions defined in equations (3.13)-(3.12) on the wave function components, I determine the a posteriori computable T matrix entries, defined in equation (3.16). An improved shooting algorithm is used to detect poles of the T matrix determinant  $\det(T)$ . The algorithm searches for roots of  $1/\det(T)$  up to a given numerical precision using fourth order numerical derivatives. Once a pole is found, depending on its position in the complex energy plane, it is interpreted according to its belonging Riemann sheet as discussed in section 3.4.

In my code I use a bottom-quark mass of  $m_b = 4977$  MeV from a quark model [129], a mass splitting between  $B$  and  $B^*$  mesons of  $\Delta m := m_{B^*} - m_B = 45$  MeV taken from the PDG ([135]) and values for the input parameters  $\alpha_5, \alpha_j, d_5, d_j$  from [72] quoted at the end of section 2.2. The Runge-Kutta solver uses a starting point of  $\hat{r}_0 = 10^{-8}$ , a maximal distance of  $r_{\max} = 2.0$  fm and step size  $\Delta \hat{r} = 0.005$ , while these parameters are carefully varied to check for numerical stability.

#### 4.1.2 Error Analysis

All results of the numerical analysis are contaminated by uncertainties. The total uncertainty of physical quantities is a combination of systematic and statistical errors. The main source of systematic errors are uncertainties in the  $\chi^2$ -fit range used to extract the potential parameters  $\alpha_5, \alpha_j, d_5, d_j$ . Another source of systematic errors are uncertainties in the temporal fit range in the effective mass plateaus used to extract the potentials  $V_5$  and  $V_j$ . These systematic errors could be estimated by varying the temporal and spatial fit ranges and calculating the corresponding physical quantities on each of them. the standard deviation of these values should give a good estimate for the resulting systematic error. Details of this procedure can be found in [63].

The main source of statistical errors is the finite number of gauge configurations used in the lattice QCD computation of the static potentials  $V_5$  and  $V_j$ . This generates an error which goes like  $1/\sqrt{N}$ , where  $N$  is the number of gauge configurations. On each configuration the static potentials  $V_5$  and  $V_j$  can be calculated from which in turn parameters  $\alpha_5, \alpha_j, d_5, d_j$  can be obtained. This gives a total number of  $N$  parameter samples  $(\alpha_5, \alpha_j, d_5, d_j)_i, i \in [1; N]$ . A good estimator for the corresponding statistical error is obtained by using resampling methods. One of such methods is the Jackknife method. This method is based on deleting values from a dataset. Let  $\{X_n\}_{n \in [1; N]}$  be a number  $N$  data points, then  $N$  reduced samples of size  $N-1$  can be obtained by deleting the  $k$ -th-value with  $k \in [1; N]$  of the data. This generates  $N$  reduced subsamples

$\{X_{n,k}\}_{n \in [1;N-1]}$ . The mean of these subsamples  $X_k$  can be defined as

$$X_k = \frac{1}{N-1} \sum_{n=1}^{N-1} X_{n,k}. \quad (4.1)$$

The resampled mean  $\hat{X}$  and the standard deviation  $\sigma_{\hat{X}}$  can be defined as

$$\hat{X} = \frac{1}{N} \sum_{k=1}^N X_k \quad (4.2)$$

$$\sigma_{\hat{X}} = \sqrt{\frac{N-1}{N} \sum_{k=1}^N (X_k - \bar{X})^2}, \quad (4.3)$$

where  $\bar{X} := \sum_{n=1}^N X_n$  is the mean of the original dataset. The final results for the quantity  $X$  can now be quoted as  $X = \hat{X} \pm \sigma_{\hat{X}}$ . The standard deviation  $\sigma_{\hat{X}}$  provides a good estimate for the statistical error.

Statistical errors are expected to be the dominant source of uncertainty. For all numerical results obtained in this work I only consider statistical errors and neglect any systematic error sources. The Jackknife method can be used to estimate statistical errors if the original sample of potentials, extracted from lattice QCD effective masses is available. If this is not the case then one has to construct the parameter samples by hand. This is done for results calculated in this work as follows. To calculate statistical errors a number of  $N = 1000$  parameter samples  $(\alpha_5, \alpha_j, d_5, d_j)$  was generated by choosing random values from distributions whose widths correspond to the statistical error of the respective parameter. Since the statistical errors of  $d_5$  is asymmetric, for  $d_5$  an asymmetric distribution was generated. The parameters of this asymmetric distribution were chosen such that the differences between the 84th and 16th percentiles and the median correspond to the lower/upper statistical uncertainty of  $d_5$ . For the parameters  $\alpha_5, \alpha_j, d_j$  gaussian distributions with a width corresponding to the standard deviation of these parameters were constructed. Physically interesting quantities like pole positions  $E_{\text{pole}}$  can be calculated on each of the parameter samples, leading to  $N$  values  $\{E_{\text{pole},n}\}_{n \in [1;N]}$ . These values form a statistical distribution on their own. With this distribution a lower statistical error  $\Delta E_{\text{pole}}^-$ , corresponding to the difference between the 84th percentile and the median and an upper statistical error  $\Delta E_{\text{pole}}^+$ , corresponding to the difference between the 16th percentile and the median are determined. Noticeably, some of the parameter samples lead to unphysical results. These outliers are removed by hand from the distribution before any further statistical analysis is conducted.

## 4.2 Pole Search in the Complex Plane

For a crude estimation of the poles of the T matrix, I apply the numerical method discussed in section 4.1.1 to a grid of complex energies  $E \in \mathbb{C}$ . I take  $\Delta \text{Re}(E) = \Delta \text{Im}(E) = 1 \text{ MeV}$  as the grid spacing. For each energy  $E \in \mathbb{C}$ , I scan for a pole like behavior of  $\det(\text{T})$ . If a signal for a pole is found in this crude scan, I then apply Newton's method with the crude pole estimate as the initial guess to find roots of  $1/\det(\text{T})$ . If convergence is achieved before a fixed number of iterations the resulting solution can be interpreted as a pole. If it turns out to be numerically stable, I interpret the pole as a physically relevant pole. Once a physically relevant pole is found, I assign a physical interpretation based on its location in the complex plane.

With the method prescribed above, I find a resonance pole on Riemann sheet III with real energy  $\text{Re}(E) - 2m_B = 94.4^{+2.9}_{-4.6} \text{ MeV}$  and width  $\Gamma = -2\text{Im}(E) = 140^{+70}_{-44} \text{ MeV}$  (see **Figure 4.1**). Numerical stability of this pole was checked by varying the numerical parameter  $r_{\text{max}}$ . No poles were found on the other Riemann sheets II and IV. The location of the pole is closer to the  $B^*B^*$  threshold than to the  $BB$  threshold. This is rather surprising, considering that without heavy spin effects a pole was found only 17 MeV above the  $BB$  threshold in [64]. The resonance energy is 4 MeV above the  $B^*B^*$  threshold and is thus generated by a combination of  $BB$  and  $B^*B^*$  scattering. The pole result entails a sizable shift of 76 MeV in the real energy compared to the single channel case in [64]. Correspondingly, this suggests that heavy spin effects have a sizable non negligible impact on the system. In the following paragraphs, I investigate the details of the effects leading to this sizable energy shift.

In equation (3.9) heavy spin effects enter via the mass splitting  $\Delta m$  and the mixing of the attractive and repulsive potentials  $V_5$  and  $V_j$ . The mixing of the static potentials is manifested in the  $2 \times 2$  potential matrix. The proportions between  $V_5$  and  $V_j$  determine the overall attractiveness in each matrix element. A numerical analysis shows that the result is largely independent of the actual value of  $V_j$ . This is a consequence of the small values of the fitting parameters  $(\alpha_j, d_j)$  compared to the values of  $(\alpha_5, d_5)$ . It thus suffices to only regard the splitting of the attractive potentials among the different components. The potential matrix defined in equation (2.25) contains a splitting of the attractive potential component into  $V_5/4$  in the (11)-component and  $3V_5/4$  in the (22)-component. Here, the (11)-component can be associated with the  $BB$  channel while the (22)-component of equation (2.25) can be associated with the  $B^*B^*$  channel. In the  $BB$  channel the attractive potential is reduced by a factor of  $1/4$ , disfavoring the existence of a resonance in this channel. In the  $B^*B^*$  channel the attractive potential is reduced only by a factor  $3/4$ , strongly favoring the existence of a resonance in this channel. The other important ingredient besides the potential matrix is the mass splitting  $\Delta m$  between the channels. The threshold energy  $E_{\text{th}} = 2m_B$  in the  $BB$  channel is about 90 MeV smaller than the threshold energy  $E_{\text{th}} = 2m_{B^*}$  in the  $B^*B^*$  channel. This increases the likelihood of a formation of a resonance in the  $BB$  channel while it lowers the likelihood of a formation of a resonance in the  $B^*B^*$  channel. The pole dynamics of the system is fully dictated by an interplay between the potential matrix and the mass splitting. In order to obtain a quantitative picture of the dominance of each of those effects, in the following subsections I study each of them individually.

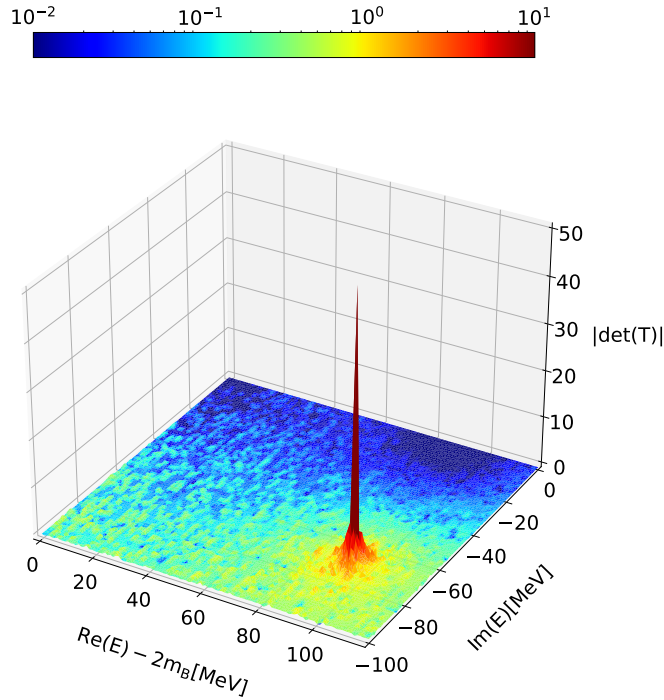


Figure 4.1: 3D plot of T matrix determinant with pole

#### 4.2.1 Rotating the potential matrix

I first address the effects of the potential matrix. To study the effect of the splitting of the attractive potential  $V_5$  and  $V_j$ , I parametrize the potential matrix by a real angle  $\theta \in [0; \pi/2]$  as

$$H_{\text{int}, 2 \times 2} = \begin{pmatrix} \cos^2 \theta V_5 + \sin^2 \theta V_j & \sin \theta \cos \theta (V_5 - V_j) \\ \sin \theta \cos \theta (V_5 - V_j) & \sin^2 \theta V_5 + \cos^2 \theta V_j \end{pmatrix}. \quad (4.4)$$

The mixing angle  $\theta$  quantifies the splitting of the attractive potential into the (11)- and (22)- component



of the potential matrix. The definition in equation 4.4 allows for a smooth transition between the single channel case from [64] which corresponds to  $\theta = 0$  and the two-channel case with heavy spin effects included defined by equation (2.24), which corresponds to  $\theta = \pi/3$ . Additionally, there is a second single-channel case for  $\theta = \pi/2$ . In this case the matrix  $H_{\text{int},2 \times 2}$  is diagonal with the repulsive potential  $V_j$  in the  $BB$  channel and the attractive potential  $V_5$  in the  $B^*B^*$  channel. By varying the angle  $\theta \in [0; \pi/2]$ , one can follow the trajectory of the resonance found in [64] in the complex energy plane. I solve equation (2.25) for each value of  $\theta$ , perform a pole scan and determine the corresponding resonance energy  $\text{Re}(\hat{E}) = \text{Re}(E) - 2m_B$  and the imaginary part  $\text{Im}(\hat{E}) = \text{Im}(E)$ . The resulting pole trajectory is shown in **Figure 4.2**. Both single-channel cases and the physical case with heavy spin effects included are highlighted by different colors.

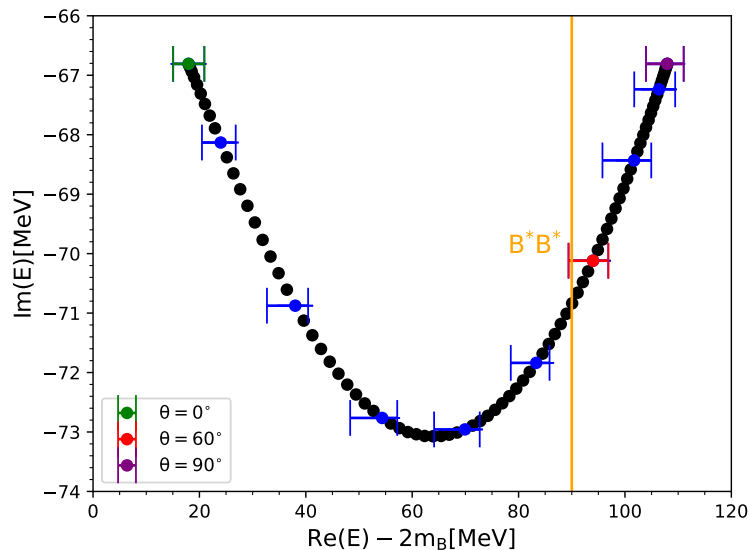


**Figure 4.2:** T matrix pole trajectory for mixing angles  $\theta \in [0^\circ; 90^\circ]$ . The vertical orange line symbolizes the  $B^*B^*$  threshold

For  $\theta = 0^\circ$  I find the pole from [64] with slightly different values for the resonance energy and width  $\Gamma$  of  $\text{Re}(E) - 2m_B = 18.0_{-6.3}^{+5.0}$  MeV and  $\Gamma = 134_{-20}^{+24}$  MeV. The discrepancy of the central values of these results compared to [64] is a consequence of different values of the reduced mass  $\mu$  used in this work and in [64]. In [64] the reduced mass is defined via the  $B$  meson mass  $\mu = m_b/2$ , while in this work I used  $\mu = m_b/2$  as the reduced mass. As expected, for  $\theta = 90^\circ$  I also find a pole with a real energy part shifted by  $2\Delta m$  but identical width  $\Gamma$ . In the range  $\theta \in [0^\circ; 36^\circ]$  I find poles with increasing real energies and increasing width. The slope of the trajectory consistently decreases in this range until a maximum in the width  $\Gamma$  is reached at  $\theta \approx 36^\circ$ . For  $\theta \in (36^\circ; 90^\circ]$  the width  $\Gamma$  decreases and the slope of the trajectory continuously increases until the single-channel case with  $\theta = 90^\circ$  is reached. The physical resonance pole at  $\theta = 60^\circ$  is included in this range. This rather unintuitive behavior of the pole trajectory can be interpreted using the potential matrix defined in equation (4.4). In the range  $\theta \in [0^\circ; 45^\circ)$  the attractive component in the  $BB$  channel outweighs the attractive component in the  $B^*B^*$  channel but continuously decreases, leading to an increase in the width  $\Gamma$  as the resonance is driven further away from the real axis. In this range the pole is located closer to the  $BB$  threshold. At  $\theta = 45^\circ$  the attractive component in the  $BB$  channel equals the attractive component in the  $B^*B^*$  and a minimum in  $\text{Im}(E)$ , corresponding to a maximum in the width  $\Gamma$  would be expected in the pole trajectory. However, in **Figure 4.2** the minimum is found at  $\theta = 36^\circ$ . The smaller angle is due to the mass splitting  $2\Delta m$  which modifies the pole trajectory. For  $\theta \in (45^\circ; 90^\circ]$  the attraction in the  $B^*B^*$  channel dominates and increases with growing angle  $\theta$ , leading to a decrease in the width because the resonance is driven towards the real axis. For  $\theta = 60^\circ$  which corresponds to the physical case the attractive potential in the  $B^*B^*$  channel is amplified by a factor of 3 compared to the attractive potential in the  $BB$  channel. This shifts the pole closer to the  $B^*B^*$  threshold, explaining the sizable shift in the real energy compared to the single channel case in [64].

Statistical errors for the real part of the energy  $\text{Re}(E) - 2m_B$  and the width  $\Gamma$  were computed with the



method discussed in section 4.1.2. In **Figure 4.2** only errors for the real part of the energy are shown. Errors were calculated for  $\theta \in \{0, 10, 20, 30, 40, 50, 60, 70, 80, 90\}^\circ$ .

### 4.2.2 Unphysical Heavy Quark Mass

Besides modifying the splitting of the attractive potential one might also think of varying the physical bottom quark mass  $m_b$ . Here, I explore the implication of varying the bottom-quark mass by a constant factor  $\kappa \in \mathbb{R}$  according to  $m_b \rightarrow \kappa m_b$ . In works in Heavy Quark Effective Theory such as [136–138] it was shown that the mass difference  $\Delta m = m_{B^*} - m_B$  is proportional to the inverse bottom-quark mass  $1/m_b$  up to order  $\mathcal{O}(1/m_b^2)$  in the bottom-quark mass  $m_b$ . The mass splitting varies with respect to the parameter  $\kappa$  according to

$$\Delta m = \frac{m_{B^*} - m_B}{\kappa} \approx \frac{45 \text{MeV}}{\kappa}. \quad (4.5)$$

With increasing  $\kappa$  the mass splitting  $\Delta m$  is reduced. This can also be thought of as an reduction in repulsion in the (22)-component of the potential matrix. For sufficiently large  $\kappa$  the attraction is expected to be strong enough to form a stable bound state. To explore this, I solved equation (3.9) for values of  $\kappa \in [1.0; 4.0]$  and performed a pole scan for each value of  $\kappa$ . In my numerical analysis I find bound states for all  $\kappa > 2.82$ , whereas for all  $\kappa \in [1.0; 2.82]$  I find resonances. The values of the binding energy  $\Delta E = \text{Re}(E) - 2m_B$  in dependence of the parameter  $\kappa$  are shown in **Figure 4.3**.

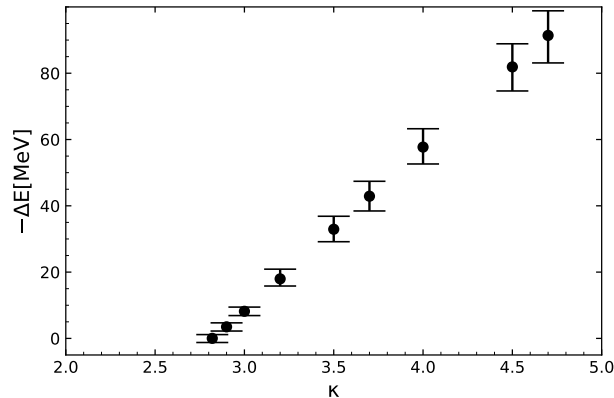


**Figure 4.3:** Binding energy  $-\Delta E := 2m_B - E$  of bound states as a function of  $\kappa$  for  $\kappa \in [2.82; 5.0]$ .

For increasing values of  $\kappa > 2.82$ , the binding energy grows nearly linearly. The value  $\kappa \approx 2.82$  at which bound states starts to appear is considerably larger compared to the single channel case for which bound states appear for all  $\kappa > 2.2$ . This deviation is a result of the shift in the real energy  $\Delta \text{Re}(E) \approx 74$  MeV between both cases which in turn results from the splitting of the attractive potential  $V_5$  between the two channels  $BB$  and  $B^*B^*$  as discussed in section 4.2.1.

To obtain a complete understanding of this deviation, I also carried out a numerical analysis of poles for various combinations of  $\theta \in [0^\circ; 90^\circ]$  and  $\kappa \in [1.0; 4.0]$  on a two dimensional grid. In total, I used  $N_\theta \times N_\kappa = 10 \times 20$  points to produce the diagram shown in **Figure 4.4**. In **Figure 4.4** I classified the different nature of poles into resonances (**blue**) and bound states (**green**). For each  $\theta$  the real part of the pole energy  $\text{Re}(E) - 2m_B$  and the width  $\Gamma$  decrease with increasing  $\kappa$ . This is due to the reduction in repulsion in the coupled-channel equation (3.9) caused by the mass splitting  $\Delta m$ . At a specific  $\kappa_{\min}$  the pole reaches the real axis at the  $BB$  threshold. For all  $\kappa > \kappa_{\min}$  the pole has  $\text{Im}(E) = 0$  with real energy  $\text{Re}(E) < 2m_B$ . The pole can now be interpreted as a bound state as shown by the green regime in **Figure 4.4**. For every angle  $\theta$  the corresponding boundary value  $\kappa_{\min}$  was obtained up to a precision of  $10^{-4}$ . The value of  $\kappa_{\min}$  continuously increases with  $\theta$  because of the increasing real part of the energy  $\text{Re}(E) - 2m_B$ . From the values  $\kappa_{\min}$  the red curve in **Figure 4.4** which marks the boundary between the two regimes was

constructed using interpolation methods.

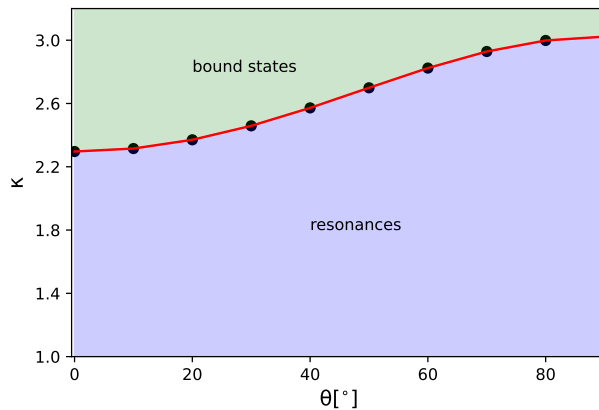


**Figure 4.4:** Different regimes of system for  $N_\theta \times N_\kappa = 10 \times 20$  combinations of  $\theta$  and  $\kappa$  with resonances marked by blue and bound states by green.

From the analysis in this section I conclude that the position and nature of a pole is determined by both the potential matrix and the heavy quark mass. Both factors contribute to a change in the pole position. Increasing  $\theta$  shifts the pole to higher real energies  $\text{Re}(E)$ , while increasing  $\kappa$  shifts it towards the real axis and lower real energies  $\text{Re}(E)$ . Out of the two the heavy quark mass seems to have more weight than the attractive potential as for every  $\theta$  poles are found for a sufficiently large  $\kappa$ .

### 4.3 Branching Ratios

Until now I have shown only numerical results for pole positions from which the mass and the width of the resonance can be extracted. In addition to pole positions it is also interesting to consider the decay structure of the resonance. The resonance discussed in section 4.2 has two decay channels. It can decay either into a  $BB$  or a  $B^*B^*$  pair. The probability of a decay into a certain channel  $\alpha$  is equivalent to the corresponding branching ratio  $BR_\alpha$ . According to [135] the branching ratio is defined as the ratio of the partial decay width  $\Gamma_\alpha$  of some decay channel  $\alpha$  and the total decay width  $\Gamma$ :

$$BR_\alpha = \frac{\Gamma_\alpha}{\Gamma}, \quad \Gamma = \sum_{\alpha} \Gamma_\alpha. \quad (4.6)$$

The partial decay widths  $\Gamma_\alpha$  can be reasonably approximated by the residues of the diagonal T matrix entries  $\text{Res}(t_{\alpha;\alpha})$ . With this, the branching ratios  $BR_\alpha$  can be approximated with the relation

$$BR_\alpha = \frac{|\text{Res}(t_{\alpha;\alpha})|}{|\text{Res}(t_{BB;BB})| + |\text{Res}(t_{B^*B^*;B^*B^*})|}, \quad \alpha \in \{BB, B^*B^*\}. \quad (4.7)$$

Thus, all one has to do to compute the branching ratios is to compute pole residues. Here, I utilize two distinct, independent methods. In the first method I use the definition of the residue as the following limit

$$\text{Res}(t_{\alpha;\alpha}) = \lim_{\epsilon \rightarrow 0} t_{\alpha;\alpha}(E_{\text{pole}} + \epsilon), \quad (4.8)$$

where  $E_{\text{pole}}$  is the corresponding pole position. Numerically, the limit  $\epsilon \rightarrow 0$  cannot be taken. The numerical result will thus have a residual dependence on the small parameter  $\epsilon$ . In practice, one has to consider several values for  $\epsilon$  and look for convergence as one approaches the pole. Depending on the singular structure of the T matrix entries  $t_{\alpha;\alpha}$  this convergence may be better or worse.

The second method considered is based on complex contour integrals. If  $\mathcal{C}$  is a closed contour around a pole at position  $E_{\text{pole}}$  and the T matrix entries  $t_{\alpha;\alpha}(E)$  are holomorphic functions of the energy  $E$  on the domain of the contour, then one can use the residue theorem to estimate the residues:

$$\text{Res}(t_{\alpha;\alpha}) = \frac{1}{2\pi i} \oint_{\mathcal{C}} t_{\alpha;\alpha}(E) dE. \quad (4.9)$$

The choice of the contour is not unique. In fact any contour without singular points is a possible choice. Yet, from a numerical point of view some contours may be better choices than others. For all calculations, I choose a small circle around the pole as the contour. This contour can be parametrized by a parameter  $\lambda \in [0; 1]$  as

$$E(\lambda) = E_{\text{pole}} + r e^{2\pi i \lambda}, \quad (4.10)$$

where  $r$  is the radius of the small circle. The choice of the radius is not unique and must be carefully investigated. However, for distances sufficiently far away from the pole the residues should not be significantly impacted by the concrete choice of  $r$ . Compared to the method defined by equation (4.8) the contour integration method is more robust to the position away from the pole provided a suitable integration path is chosen. We note that the parametrization defined by equation (4.10) works only for poles which are not located on a branch cut. For such poles a circle will not be a suitable choice, because  $t_{\alpha;\alpha}(E)$  is not holomorphic on the branch cut. Numerically, the contour integration method is more expensive, because instead of computing the T matrix entries  $t_{\alpha;\alpha}(E)$  at a single point as in the limit-method one needs to compute its values along a predefined integration path. The numerical cost depends on the integration method and the number of integration points on the contour.

I computed residues with the first method for multiple  $\epsilon \in \{10^{-4}, 10^{-5}, 10^{-6}, 10^{-7}, 10^{-8}, 10^{-9}\}$  and  $\theta \in [0^\circ; 90^\circ]$ . I find reasonable convergence for  $\epsilon \in \{10^{-7}, 10^{-8}, 10^{-9}\}$  (see Appendix D). In the left panel of **Figure 4.5** I show results for the branching ratios for  $\epsilon = 10^{-8}$ .

I also computed residues with the contour-integration method. To investigate the dependence on the radius  $r$ , I computed residues for  $r \in \{0.5, 0.8, 1.0, 1.2, 1.4, 1.6, 1.8, 2.0\}$  MeV. As expected I observe smaller deviations than for the limit-method when varying  $\epsilon$  (see Appendix D). Residues were computed for angles  $\theta \in \{0^\circ, 10^\circ, 20^\circ, 30^\circ, 40^\circ, 50^\circ, 60^\circ, 70^\circ, 80^\circ, 90^\circ\}$ . For the estimations of the central values I used  $N = 30$  integration steps, while for a crude estimation of the errors I used only  $N = 10$  integration steps. In the right panel of **Figure 4.5** I show my results for the branching ratios for  $r = 1$  MeV with this method and the relative difference compared to the limit-method with  $\epsilon = 10^{-8}$ .

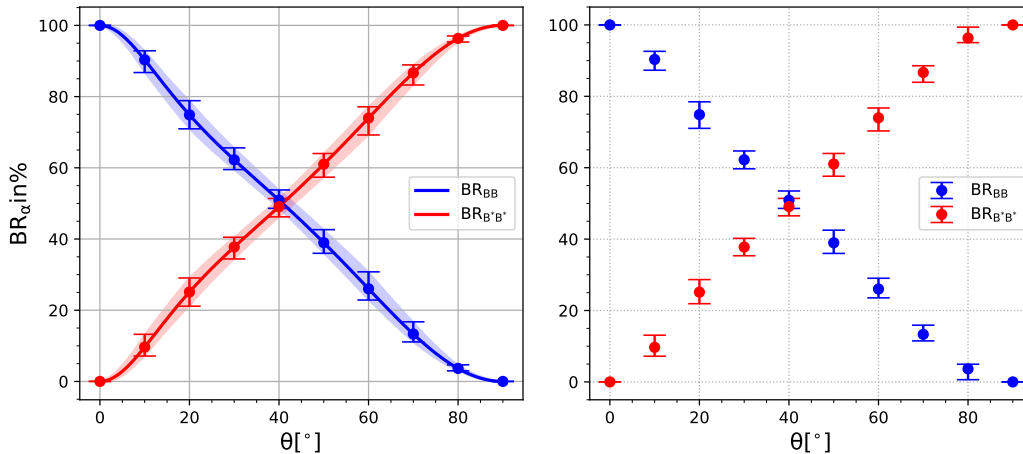


**Figure 4.5:** (left):  $BB$  and  $B^*B^*$  Branching ratios calculated with the limit-method with  $\epsilon = 10^{-8}$ , (right):  $BB$  and  $B^*B^*$  Branching ratios calculated with the contour integration-method with  $r = 1$  MeV

For  $\theta = 0^\circ$ , i.e. where both channels are decoupled the branching ratio in the  $BB$  channel is almost 100% in the left and right panels in **Figure 4.5**. For this case the resonance decays with high probability into the  $BB$  channel, because the attractive potential is fully located in the  $BB$  channel. For  $\theta > 0^\circ$  the  $BB$  branching ratio continuously decreases, whereas the  $B^*B^*$  branching ratio continuously increases. This a consequence of

the increasing proportion of the attractive potential in the  $B^*B^*$  channel. At  $\theta \approx 41^\circ$ , where the proportions of the attractive potential are almost equal the branching ratio of the  $B^*B^*$  channel becomes higher than the branching ratio of the  $BB$  channel. For  $\theta \in (41^\circ; 90^\circ]$  the system then couples predominantly to the  $B^*B^*$  decay channel. For  $\theta = 90^\circ$ , where again both channels are decoupled the branching ratio of the  $B^*B^*$  channel is almost 100%. The system now decays almost exclusively into a  $B^*B^*$  pair, since the attractive potential is fully located in the  $B^*B^*$  channel. This behavior of the branching ratio is identical for the limit-method and the contour-integration method. In fact, the numerical difference between values calculated with both methods does not exceed a maximal difference of  $2 \cdot 10^{-2}$  %. For the physical angle  $\theta = 60^\circ$  the branching ratios are  $BR_{BB} = 26^{+3}_{-2}$  % and  $BR_{B^*B^*} = 74^{+3}_{-4}$  %. Here, I quote the branching ratios computed with the contour integration method. For the physically relevant case  $\theta = 60^\circ$ , I conclude that the probability that the resonance decays into a  $B^*B^*$  is much higher than the probability it decays into a  $BB$  pair. In other terms, this indicates a stronger coupling of the resonance to the  $B^*B^*$  than to the  $BB$  channel.

## 4.4 Coupled-Channel Eigenphases

In section 3.3, I showed how to compute the eigenphases for a coupled channel scattering problem. There, I found the following relation between the two eigenphases  $\delta_\alpha(E)$ ,  $\alpha \in \{1, 2\}$  and the two S matrix eigenvalues  $s_\alpha$ ,  $\alpha \in \{1, 2\}$

$$s_\alpha = e^{2i\delta_\alpha(E)}, \quad (4.11)$$

where the eigenvalues  $s_\alpha$  with  $\alpha \in \{1, 2\}$  must be evaluated at real energies  $E \in \mathbb{R}$ . To compute the eigenvalues  $s_\alpha$  with  $\alpha \in \{1, 2\}$ , I solve equation (3.9) for real energies  $\tilde{E} \in [0; 300]$  MeV. The resulting eigenvalues  $s_\alpha$  can be inserted into equation (4.11) to compute the two eigenphases  $\delta_\alpha(E)$ .

However, there is one important caveat in the numerical analysis which must be taken care of. At the two branch points, corresponding to the thresholds  $E_{\text{th},i} \in \{2m_B, 2m_{B^*}\}$  the corresponding real channel momentum  $k_i$  vanishes. This introduces an instability into the numerical procedure since the hankel function  $h_1^{(1)}(k_i r)$  diverges for  $k_i = 0$ . I resolve this issue by using a complex energy  $E \in \mathbb{C}$  with an arbitrary small non zero imaginary part. In my numerical calculation I used an imaginary energy part of  $\text{Im}(E) = 10^{-7}$  MeV which does not significantly alter the result. The resulting phase shifts are shown in **Figure 4.6** together with the single-channel phase shifts for  $\theta = 0^\circ$  and  $\theta = 90^\circ$ .

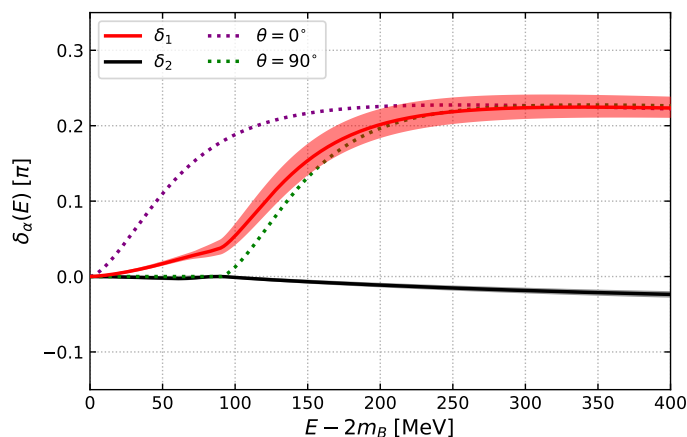


**Figure 4.6:** Coupled channel eigenphases for energies  $E - 2m_B \in [0 \text{ MeV}; 400 \text{ MeV}]$

For  $\theta = 0^\circ$  I obtain the phase shift found in [64] with a continuous rise from 0 to  $\pi/4$  as indicated by the purple dotted curve in **Figure 4.6**. In the single-channel case the off diagonal elements of the T matrix vanish which leads to only one non vanishing eigenphase  $\delta_1$ . This eigenphase can be fully associated with the  $BB$  channel. For the single channel case for  $\theta = 90^\circ$  the same phase shift as for  $\theta = 0^\circ$  shifted by an energy of 90 MeV can be found, corresponding to the  $B^*B^*$  threshold as shown by the green dotted curve in **Figure 4.6**. As for  $\theta = 0^\circ$  there is only one non vanishing eigenphase  $\delta_2$  fully associated with the  $B^*B^*$  channel. In **4.6** one can notice a small discontinuity at  $E - 2m_B = 90$  MeV. This is due to the right hand

cut introduced by the  $B^*B^*$  threshold which lies on the real energy axis. I already discussed this caveat at the beginning of this subsection. For the physical case with  $\theta = 60^\circ$  I observe that the eigenphase  $\delta_1$  dominates. In contrast to the single-channel cases for the coupled-channel case the eigenphases reflect a mix of the two channels  $BB$  and  $B^*B^*$ . Thus, the eigenphases can not be associated uniquely with one of the two channels. For energies  $E < 2m_{B^*}$  the eigenphase  $\delta_1$  increases linearly while the eigenphase  $\delta_2$  decreases. In the vicinity of the  $B^*B^*$  threshold the phase  $\delta_1$  exhibits a small jump, again caused by the branch cut at  $E = 2m_{B^*}$ . For energies  $E > 2m_{B^*}$  the eigenphase  $\delta_1$  monotonically increases until it converges to the single-channel phase shift with  $\delta_1 \approx \pi/4$  at high energies. The other eigenphase  $\delta_2$  decreases until it saturates at  $\delta_2 \approx -0.02 \pi$  at high energies. Compared to the single-channel case in [64] the entire curve of the eigenphase  $\delta_1$  is shifted towards higher energies. This may be a consequence of the increasing real parts of the pole energies  $\text{Re}(E_{\text{Pole}})$  for increasing mixing angle  $\theta$  shown in **Figure 4.2**. Based on this observation, I conclude that heavy spin effects manifest in a rightward shift in the eigenphase towards higher energies which is in line with the shift of the real part of the pole position.

With this reasoning the discussion of this section and the entire chapter is concluded.

## Chapter 5

# Conclusion and Outlook

In this thesis, I studied heavy spin effects in the  $\bar{b}b\bar{u}d$  tetraquark resonance with quantum numbers  $I(J^P) = 0(1^-)$ . I developed a two-channel scattering formalism to describe the coupling between  $BB$  and  $B^*B^*$  channels. Based on this formalism, I conducted a numerical study of the system. With the refined scattering formalism I find a resonance pole at  $\text{Re}(E) - 2m_B = 94.4_{-4.6}^{+2.9}$  MeV and width  $\Gamma = 140_{-44}^{+70}$  MeV. The real part of the pole energy is located only 4MeV above the  $B^*B^*$  threshold. This suggests that the resonance is located close to the  $B^*B^*$  threshold, rather than close to the  $BB$  threshold as previously thought. The sizable shift in the real part of the pole energy compared to the single-channel case in [64, 65] was found to be a consequence of an interplay between the mass splitting and the splitting of the attractive potential. In addition, I also computed the branching ratios for the two decay channels  $BB$  and  $B^*B^*$ . I find branching ratios of  $BR_{BB} = 26_{-2}^{+3}$  % and  $BR_{B^*B^*} = 74_{-4}^{+3}$  %. This result indicates a stronger coupling of the resonance to the  $B^*B^*$  decay channel than to the  $BB$  channel. While the probability that the resonance decays into a  $B^*B^*$  is approximately three times as large as the probability it decays into a  $BB$  pair, the coupling to the  $BB$  pair is still sizable and cannot be neglected. Thus, I conclude that coupled channel effects are important and non negligible. Based on these results, I find evidence for a resonance close to the  $B^*B^*$  threshold which is coupled to both channels  $BB$  and  $B^*B^*$ . However, this result should still be treated with caution as the approach used in this work suffers from a number of systematic errors which are not easily quantifiable.

The approach is severely limited by the static approximation. In the real world heavy quarks are not static, leading to higher order corrections of the potential. The result of this work may be improved by considering also  $\mathcal{O}(1/m_b)$  or even higher order corrections to the static potentials (see [58, 139, 140]). Also, the quality of the static potentials is limited by the small number of lattice data points calculated in [72]. This leads to an additional systematic error for the results of this work. A newer calculation of the static potentials with improved lattice QCD methods is currently ongoing. Another limitation comes from integrating out all light degrees of freedom. This prohibits the study of scattering channels like  $BB\pi$  whose threshold lies comparatively close to the  $B^*B^*$  threshold. For resonances close to the  $B^*B^*$  threshold the contribution of the three-particle  $BB\pi$  channel may be non negligible anymore.

Because of these limitations, the main results of this work must be looked upon as qualitative. Ultimately, a coupled-channel finite-volume lattice QCD study in the sense of [37] would be desirable to settle the physics of the  $\bar{b}b\bar{u}d$  resonance. Ideally, this study should include mixing between two- and three particle scattering channels to include also the  $BB\pi$  channel. In addition, also a consistent treatment of the left-hand cut generated by one- and two-pion exchange is needed(see [141–143]). The  $\bar{b}b\bar{u}d, I(J^P) = 0(1^-)$  system may suit as a playground for different methods to resolve the left-hand cut problem. The knowledge gained in this work may be used as a starting point to build the setup for such a finite-volume lattice QCD study. The results of such a study can then be compared to experiment. At the end, only experiment will reveal the fate of the resonance in the real world.

## Appendix A

# Dimensionless Quantities

In the following table all conversions between dimensionful quantities  $q$  and dimensionless quantities  $\hat{q}$  are provided. The lattice spacing in fm is denoted as  $a$  and the lattice spacing in 1/MeV is denoted as  $a_{\text{MeV}}$ . both lattice spacings can be converted into each other using the planck constant  $\hbar$  and the speed of light  $c$

$$a_{\text{MeV}} = \frac{a}{\hbar c} \quad (\text{A.1})$$

with  $\hbar c \approx 197.3 \text{ MeVfm}$

$q$	$\hat{q}$
$r$	$\hat{r} := r/a$
$k$	$\hat{k} := k \cdot a_{\text{MeV}}$
$\tilde{E}$	$\hat{\tilde{E}} := 2\mu a_{\text{MeV}}^2 \tilde{E}$
$V_5$	$\hat{V}_5 := 2\mu a_{\text{MeV}}^2 V_5$
$V_j$	$\hat{V}_j := 2\mu a_{\text{MeV}}^2 V_j$

**Table A.1:** Conversions between dimensionful quantities  $q$  and dimensionless quantities  $\hat{q}$

## Appendix B

# Conservation of Orbital Angular Momentum

Here, I show that the orbital angular momentum  $\mathbf{L}$  is conserved. This is equivalent to showing that  $\mathbf{L}^2$  commutes with the  $16 \times 16$  Hamiltonian  $H$  whose parts are defined in equations (2.12) and (2.13). The components  $H_{ij}$ ,  $i, j \in [1; 16]$  of this Hamiltonian in the center-of-mass frame read

$$H_{ij} = M_{ij} - \frac{1}{2\mu} \left[ \frac{\partial^2}{\partial r^2} + \frac{2}{r} \frac{\partial}{\partial r} - \frac{\mathbf{L}^2}{r^2} \right] \delta_{ij} + H_{\text{int},ij}(r), \quad (\text{B.1})$$

where  $M_{ij} := (M \otimes \mathbb{1}_{4 \times 4} + \mathbb{1}_{4 \times 4} \otimes M)_{ij}$  is a  $16 \times 16$  matrix which contains combinations of  $B$  and  $B^*$  masses.

I now calculate the commutator  $[\mathbf{L}^2, H_{ij}]$  for each component of the Hamiltonian  $H$  :

$$[\mathbf{L}^2, H_{ij}] = [\mathbf{L}^2, M_{ij}] - \frac{1}{2\mu} \left[ \mathbf{L}^2, \frac{\partial^2}{\partial r^2} + \frac{2}{r} \frac{\partial}{\partial r} \right] + \frac{1}{2\mu} \left[ \mathbf{L}^2, \frac{\mathbf{L}^2}{r^2} \right] + [\mathbf{L}^2, H_{\text{int},ij}(r)]. \quad (\text{B.2})$$

Here, the interaction term of the Hamiltonian  $H_{\text{int}}$  depends only on the radial coordinate  $r$ . The commutator  $\left[ \mathbf{L}^2, \frac{\mathbf{L}^2}{r^2} \right]$  can be further simplified as

$$\left[ \mathbf{L}^2, \frac{\mathbf{L}^2}{r^2} \right] = \frac{1}{r^2} \underbrace{[\mathbf{L}^2, \mathbf{L}^2]}_{=0} + \mathbf{L}^2 \left[ \mathbf{L}^2, \frac{1}{r^2} \right] = \mathbf{L}^2 \left[ \mathbf{L}^2, \frac{1}{r^2} \right]. \quad (\text{B.3})$$

The first term in equation (B.2) is trivially zero, because  $M_{ij}$  contains only constant numbers. The remaining terms contain commutators of the form

$$\left[ \mathbf{L}^2, \frac{\partial^n}{\partial r^n} \right], \quad n \in \{1, 2\} \quad \text{and} \quad [\mathbf{L}^2, F(r)], \quad (\text{B.4})$$

where  $F(r)$  are the values of a function  $F$  that only depends on the radial coordinate. Thus, in order to show that  $[\mathbf{L}^2, H_{ij}] = 0$  it suffices to prove that the two commutators in (B.4) vanish.

The angular momentum operator squared  $\mathbf{L}^2$  can be expressed via the  $\theta$ - and  $\varphi$  derivatives as

$$\mathbf{L}^2 = \frac{1}{\sin \theta} \frac{\partial}{\partial \theta} \left( \sin \theta \frac{\partial}{\partial \theta} \right) + \frac{1}{\sin^2 \theta} \frac{\partial^2}{\partial \varphi^2}. \quad (\text{B.5})$$

Moreover, the following relations found in standard textbooks hold for derivatives and coordinates  $\theta, \varphi$

$$\left[ \frac{\partial^m}{\partial \theta_i^m}, \frac{\partial^n}{\partial r^n} \right] = 0, \quad \theta_i \in \{\theta, \varphi\}, \quad m, n \in \mathbb{N} \quad (\text{B.6})$$

$$\left[ \Theta(\theta_i), \frac{\partial^n}{\partial r^n} \right] = 0, \quad \theta_i \in \{\theta, \varphi\}, \quad m, n \in \mathbb{N}, \quad (\text{B.7})$$

where  $\Theta$  is a  $\theta_i$ -dependent function which is analytic in  $\theta_i$ .

Hence, I conclude that all commutators of the form  $[\mathbf{L}^2, \frac{\partial^n}{\partial r^n}]$  are zero. The second commutator of equation



(B.4) is more complicated, because it contains arbitrary radial functions  $F$ . To calculate this commutator it is most useful to consider it pointwise. For analytic functions  $F$  values of this function in the vicinity of a given point  $r_0 \in (0; \infty)$  can be expanded around this point with a series expansion.

Let  $r_0 \in (0; \infty)$  and  $r \in B_\epsilon(r_0)$ , where  $B_\epsilon(r_0)$  is a ball of small radius  $\epsilon$  around  $r_0$ , then for every point  $r \in B_\epsilon(r_0)$

$$F(r) = \sum_{n=0}^{\infty} c_n (r - r_0)^n, \quad (\text{B.8})$$

where  $c_n \in \mathbb{R}$  are real coefficients. For analytic functions  $F$  the commutator (B.4) can be rewritten for  $r \in B_\epsilon(r_0)$  as

$$\begin{aligned} [\mathbf{L}^2, F(r)] &= \sum_{n=0}^{\infty} c_n [\mathbf{L}^2, (r - r_0)^n] = \sum_{n=0}^{\infty} c_n \left[ \frac{1}{\sin \theta} \frac{\partial}{\partial \theta} \left( \sin \theta \frac{\partial}{\partial \theta} \right) + \frac{1}{\sin^2 \theta} \frac{\partial^2}{\partial \varphi^2}, (r - r_0)^n \right] \\ &= \sum_{n=0}^{\infty} c_n \left( \left[ \frac{\partial^2}{\partial \theta^2}, (r - r_0)^n \right] + \left[ \frac{\partial}{\partial \theta} \left( \sin \theta \frac{\partial}{\partial \theta} \right), (r - r_0)^n \right] + \left[ \frac{1}{\sin^2 \theta} \frac{\partial^2}{\partial \varphi^2}, (r - r_0)^n \right] \right). \end{aligned} \quad (\text{B.9})$$

It is well known from standard textbooks that a coordinate  $\theta_1$  commutes with a derivative with respect to a different coordinate  $\theta_2$  if the basis vectors associated to these coordinates are perpendicular. The spherical coordinates  $(r, \theta, \varphi)$  form an orthonormal coordinate basis, because their basis vectors  $\vec{e}_i$  fulfill the relation  $\vec{e}_i \cdot \vec{e}_j = \delta_{ij}$  with  $i, j \in \{r, \theta, \varphi\}$ . Consequently the following relations hold for spherical coordinates

$$\left[ \frac{\partial^m}{\partial \theta_i^m}, r^n \right] = 0, \quad \theta_i \in \{\theta, \varphi\}, m, n \in \mathbb{N} \quad (\text{B.10})$$

$$[\Theta(\theta_i), r^n] = 0, \quad \theta_i \in \{\theta, \varphi\}, m, n \in \mathbb{N} \quad (\text{B.11})$$

for analytic functions  $\Theta$ . All commutators in equation (B.9) correspond to one of these two commutators. I thus conclude that for analytic functions  $F$  all terms in equation (B.9) vanish and  $[\mathbf{L}^2, F(r)] = 0$  pointwise for all  $r \in (0; \infty)$ . The functions  $F_1 : r \mapsto 1/r^2$  and  $H_{\text{int},ij}$  are both analytic on  $r \in (0, \infty)$ , correspondingly

$$\left[ \mathbf{L}^2, \frac{1}{r^2} \right] = [\mathbf{L}^2, H_{\text{int},ij}] = 0 \quad (\text{B.12})$$

and the commutator  $[\mathbf{L}^2, H_{\text{int},ij}] = 0$ . This implies that orbital angular momentum is a conserved quantity of the system studied in this work. With this ascertainment the proof contained in this section is completed.

## Appendix C

# Derivation of the Unitarity Constraint

Here, I derive the unitarity constraint for the single-channel scattering amplitude  $\mathbf{T}$ . The starting point of this derivation is the unitarity condition for the single-channel S matrix  $\mathbf{S} \in U(1)$

$$\mathbf{S}^* \mathbf{S} = 1. \quad (\text{C.1})$$

The S matrix relates to the scattering amplitude  $\mathbf{T}$  as

$$\mathbf{S} = 1 + 2i\mathbf{T}. \quad (\text{C.2})$$

By using equation (C.2) equation (C.1) can be expressed by  $\mathbf{T}$  as follows

$$\begin{aligned} \mathbf{S}^* \mathbf{S} &= (1 + 2i\mathbf{T})^* (1 + 2i\mathbf{T}) = (1 - 2i\mathbf{T}^*) (1 + 2i\mathbf{T}) = 1 + 2i(\mathbf{T} - \mathbf{T}^*) + 4\mathbf{T}^* \mathbf{T} \\ &= 1 - 4\text{Im}(\mathbf{T}) + 4|\mathbf{T}|^2 = 1 + 4(|\mathbf{T}|^2 - \text{Im}(\mathbf{T})) = 1, \end{aligned} \quad (\text{C.3})$$

where the relation  $\mathbf{T} - \mathbf{T}^* = 2i\text{Im}(\mathbf{T})$  was used. With equation (C.3) the unitarity condition becomes

$$1 + 4(|\mathbf{T}|^2 - \text{Im}(\mathbf{T})) = 1. \quad (\text{C.4})$$

This equation is only fulfilled if the expression in the bracket vanishes. This leads to the unitarity constraint

$$\text{Im}(\mathbf{T}) = |\mathbf{T}|^2. \quad (\text{C.5})$$

This completes the derivation of the unitarity constraint for the single-channel scattering amplitude  $\mathbf{T}$ . For energies  $E \in \mathbb{C}$  close to the pole  $\mathbf{T}$  can be parametrized according to equation (3.26):

$$\mathbf{T} = -\frac{\Gamma/2}{E - m \pm i\Gamma/2}, \quad (\text{C.6})$$

where the minus sign in the denominator is used for energies  $E$  on Riemann sheet I, while the plus sign is used for energies  $E$  on Riemann sheet II. equation (C.6) can now be inserted into the left- and right hand side of equation (C.5). For this it is first useful to rewrite  $\mathbf{T}$  as

$$\mathbf{T} = -\frac{\Gamma/2(E - m \mp i\Gamma/2)}{(E - m \pm i\Gamma/2)(E - m \mp i\Gamma/2)} = -\frac{\Gamma/2(E - m)}{(E - m)^2 + \Gamma^2/4} \pm i\frac{\Gamma^2/4}{(E - m)^2 + \Gamma^2/4}. \quad (\text{C.7})$$

The left hand side of equation (C.6) then yields

$$\text{Im}(\mathbf{T}) = \pm \frac{\Gamma^2/4}{(E - m)^2 + \Gamma^2/4}. \quad (\text{C.8})$$

For the right hand side of equation (C.6) I obtain

$$|\mathbf{T}|^2 = \frac{\Gamma^2/4}{(E - m)^2 + \Gamma^2/4}. \quad (\text{C.9})$$

Equating both sides leads to the equation

$$\frac{\Gamma^2/4}{(E-m)^2 + \Gamma^2/4} = \pm \frac{\Gamma^2/4}{(E-m)^2 + \Gamma^2/4} \quad (\text{C.10})$$

Evidently for  $\Gamma \neq 0$  this equation is only fulfilled if the plus sign is chosen. the plus sign corresponds to poles on Riemann sheet II. Consequently in the single-channel case only poles on Riemann sheet II satisfy the unitarity constraint. Hence, all resonances are located on Riemann sheet II.

## Appendix D

# Convergence of Branching Ratios

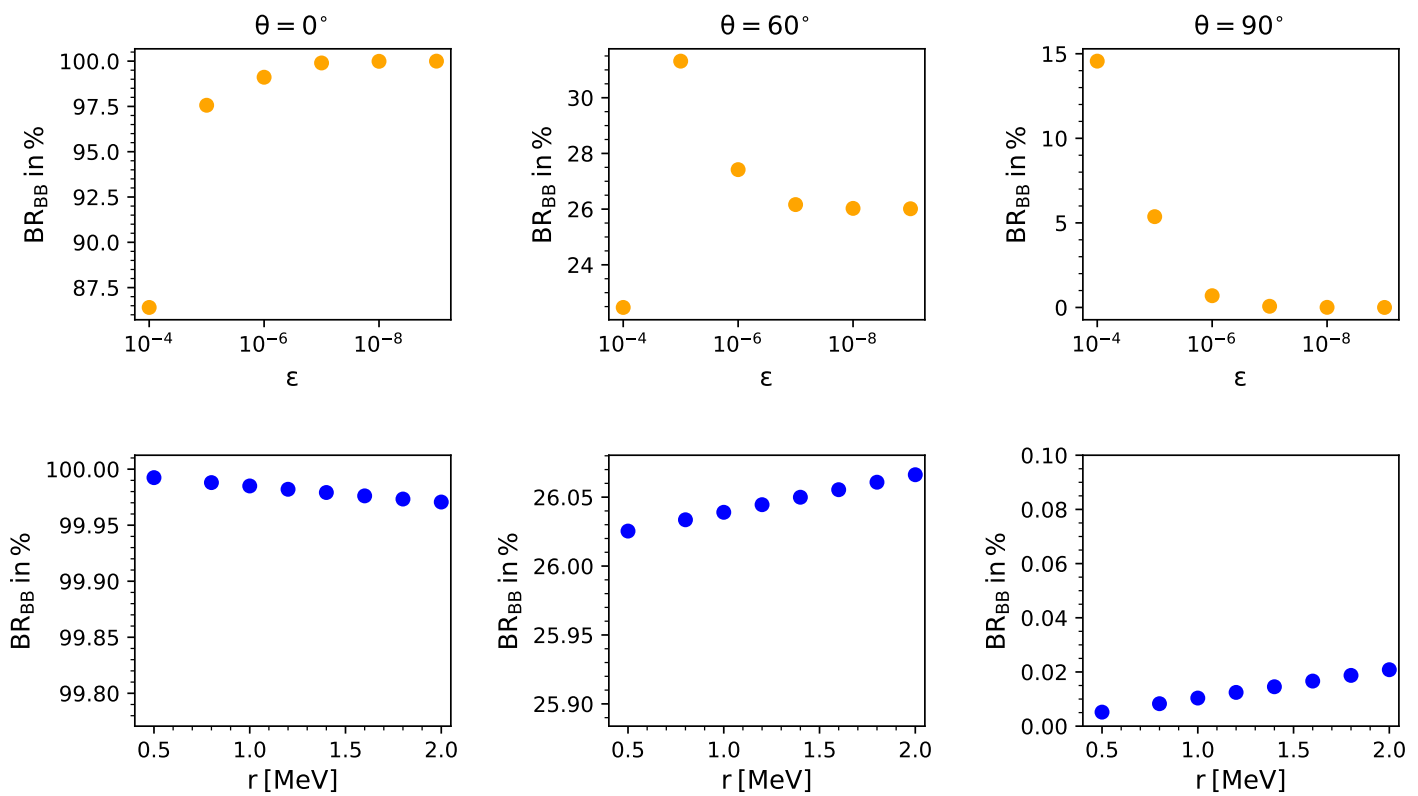


**Figure D.1:** (upper row):  $BB$  Branching ratio calculated with limit-method for  $\theta \in \{0^\circ, 60^\circ, 90^\circ\}$  as a function of  $\epsilon$ , (lower row):  $BB$  and  $B^*B^*$  Branching ratios calculated with contour integration-method for  $\theta \in \{0^\circ, 60^\circ, 90^\circ\}$  as a function of  $r$

# Acknowledgements

The completion of this thesis would not have been possible without the help of a couple of people. This thesis was conducted under the supervision of Marc Wagner. I thank Marc for his continuous support during the last years, for guidance, for intriguing discussions and also at times much needed suggestions for improvement. I express my deepest gratitude to my parents for raising me, supporting me throughout all the years of my physics studies and for providing me with all the necessary material, when I needed it, whether it was books or electronic devices like a new computer. On that note, I also want to thank my brother Anton for being there to have my back. I also want to thank all my friends who have supported me in the past or are currently supporting me. Particularly, I express my gratitude to Joshua Lin from MIT for proof reading an earlier version of this thesis and providing helpful comments. At last, I want to thank Owe Philipsen for being the second supervisor of this thesis.

I close this thesis with a quote from my personal physics role model Richard P. Feynman:

“We seem gradually to be groping toward an understanding of the world of subatomic particles, but we really do not know how far we have yet to go in this task.” – R. P. Feynman

# Bibliography

- [1] D. Acosta et al. “Observation of the narrow state  $X(3872) \rightarrow J/\psi\pi^+\pi^-$  in  $\bar{p}p$  collisions at  $\sqrt{s} = 1.96$  TeV”. In: *Phys. Rev. Lett.* 93 (2004), p. 072001. DOI: 10.1103/PhysRevLett.93.072001. arXiv: hep-ex/0312021.
- [2] Roel Aaij et al. “Observation of an exotic narrow doubly charmed tetraquark”. In: *Nature Phys.* 18.7 (2022), pp. 751–754. DOI: 10.1038/s41567-022-01614-y. arXiv: 2109.01038 [hep-ex].
- [3] Xiao-Yun Wang et al. “Discovery potential for the LHCb fully-charm tetraquark  $X(6900)$  state via  $\bar{p}p$  annihilation reaction”. In: *Phys. Rev. D* 102 (2020), p. 116014. DOI: 10.1103/PhysRevD.102.116014. arXiv: 2007.09697 [hep-ph].
- [4] Roel Aaij et al. “Observation of structure in the  $J/\psi$ -pair mass spectrum”. In: *Sci. Bull.* 65.23 (2020), pp. 1983–1993. DOI: 10.1016/j.scib.2020.08.032. arXiv: 2006.16957 [hep-ex].
- [5] M. Ablikim et al. “Observation of a Vector Charmoniumlike State at 4.7 GeV/c<sup>2</sup> and Search for  $Z_{cs}$  in  $e^+e^- \rightarrow K^+K^-J/\psi$ ”. In: *Phys. Rev. Lett.* 131.21 (2023), p. 211902. DOI: 10.1103/PhysRevLett.131.211902. arXiv: 2308.15362 [hep-ex].
- [6] Roel Aaij et al. “Evidence for an  $\eta_c(1S)\pi^-$  resonance in  $B^0 \rightarrow \eta_c(1S)K^+\pi^-$  decays”. In: *Eur. Phys. J. C* 78.12 (2018), p. 1019. DOI: 10.1140/epjc/s10052-018-6447-z. arXiv: 1809.07416 [hep-ex].
- [7] Medina Ablikim et al. “Observation of a Near-Threshold Structure in the  $K^+$  Recoil-Mass Spectra in  $e^+e^- \rightarrow K^+(D_s^-D^{*0} + D_s^{*-}D^0)$ ”. In: *Phys. Rev. Lett.* 126.10 (2021), p. 102001. DOI: 10.1103/PhysRevLett.126.102001. arXiv: 2011.07855 [hep-ex].
- [8] Roel Aaij et al. “Amplitude analysis of the  $B^+ \rightarrow D^+D^-K^+$  decay”. In: *Phys. Rev. D* 102 (2020), p. 112003. DOI: 10.1103/PhysRevD.102.112003. arXiv: 2009.00026 [hep-ex].
- [9] Medina Ablikim et al. “Amplitude analysis and branching fraction measurement of  $D_s^+ \rightarrow K^+K^-\pi^+$ ”. In: *Phys. Rev. D* 104.1 (2021), p. 012016. DOI: 10.1103/PhysRevD.104.012016. arXiv: 2011.08041 [hep-ex].
- [10] Roel Aaij et al. “Model-independent confirmation of the  $Z(4430)^-$  state”. In: *Phys. Rev. D* 92.11 (2015), p. 112009. DOI: 10.1103/PhysRevD.92.112009. arXiv: 1510.01951 [hep-ex].
- [11] M. Ablikim et al. “Observation of an Isoscalar Resonance with Exotic JPC=1-+ Quantum Numbers in  $J/\psi \rightarrow \gamma\eta\eta$ ”. In: *Phys. Rev. Lett.* 129.19 (2022). [Erratum: Phys.Rev.Lett. 130, 159901 (2023)], p. 192002. DOI: 10.1103/PhysRevLett.129.192002. arXiv: 2202.00621 [hep-ex].
- [12] M. Ablikim et al. “Partial wave analysis of  $J/\psi \rightarrow \gamma\eta\eta$ ”. In: *Phys. Rev. D* 106.7 (2022). [Erratum: Phys.Rev.D 107, 079901 (2023)], p. 072012. DOI: 10.1103/PhysRevD.106.072012. arXiv: 2202.00623 [hep-ex].
- [13] M. Ablikim et al. “Confirmation of a charged charmoniumlike state  $Z_c(3885)^\mp$  in  $e^+e^- \rightarrow \pi^\pm(D\bar{D}^*)^\mp$  with double  $D$  tag”. In: *Phys. Rev. D* 92.9 (2015), p. 092006. DOI: 10.1103/PhysRevD.92.092006. arXiv: 1509.01398 [hep-ex].
- [14] M. Ablikim et al. “Observation of a charged  $(D\bar{D}^*)^\pm$  mass peak in  $e^+e^- \rightarrow \pi D\bar{D}^*$  at  $\sqrt{s} = 4.26$  GeV”. In: *Phys. Rev. Lett.* 112.2 (2014), p. 022001. DOI: 10.1103/PhysRevLett.112.022001. arXiv: 1310.1163 [hep-ex].
- [15] Roel Aaij et al. “Observation of the resonant character of the  $Z(4430)^-$  state”. In: *Phys. Rev. Lett.* 112.22 (2014), p. 222002. DOI: 10.1103/PhysRevLett.112.222002. arXiv: 1404.1903 [hep-ex].
- [16] T. Xiao et al. “Observation of the Charged Hadron  $Z_c^\pm(3900)$  and Evidence for the Neutral  $Z_c^0(3900)$  in  $e^+e^- \rightarrow \pi\pi J/\psi$  at  $\sqrt{s} = 4170$  MeV”. In: *Phys. Lett. B* 727 (2013), pp. 366–370. DOI: 10.1016/j.physletb.2013.10.041. arXiv: 1304.3036 [hep-ex].
- [17] M. Ablikim et al. “Study of  $e^+e^- \rightarrow \pi^0 X(3872)\gamma$  and search for  $Z_c(4020)^0 \rightarrow X(3872)\gamma$ ”. In: *Phys. Rev. D* 104 (2021), p. 012001. DOI: 10.1103/PhysRevD.104.012001. arXiv: 2102.00644 [hep-ex].
- [18] M. Ablikim et al. “Observation of a Charged Charmoniumlike Structure in  $e^+e^- \rightarrow \pi^+\pi^-J/\psi$  at  $\sqrt{s} = 4.26$  GeV”. In: *Phys. Rev. Lett.* 110 (2013), p. 252001. DOI: 10.1103/PhysRevLett.110.252001. arXiv: 1303.5949 [hep-ex].

- [19] M. Ablikim et al. “Observation of a Charged Charmoniumlike Structure  $Z_c(4020)$  and Search for the  $Z_c(3900)$  in  $e^+e^- \rightarrow \pi^+\pi^-h_c$ ”. In: *Phys. Rev. Lett.* 111.24 (2013), p. 242001. DOI: 10.1103/PhysRevLett.111.242001. arXiv: 1309.1896 [hep-ex].
- [20] A. Bondar et al. “Observation of two charged bottomonium-like resonances in  $Y(5S)$  decays”. In: *Phys. Rev. Lett.* 108 (2012), p. 122001. DOI: 10.1103/PhysRevLett.108.122001. arXiv: 1110.2251 [hep-ex].
- [21] Serguei Chatrchyan et al. “Observation of a Peaking Structure in the  $J/\psi\phi$  Mass Spectrum from  $B^\pm \rightarrow J/\psi\phi K^\pm$  Decays”. In: *Phys. Lett. B* 734 (2014), pp. 261–281. DOI: 10.1016/j.physletb.2014.05.055. arXiv: 1309.6920 [hep-ex].
- [22] Claude W. Bernard et al. “Exotic mesons in quenched lattice QCD”. In: *Phys. Rev. D* 56 (1997), pp. 7039–7051. DOI: 10.1103/PhysRevD.56.7039. arXiv: hep-lat/9707008.
- [23] Jan Oliver Daldrop et al. “Lattice investigation of the tetraquark candidates  $a_0(980)$  and  $\kappa$ ”. In: *PoS LATTICE2012* (2012). Ed. by Derek Leinweber et al., p. 161. DOI: 10.22323/1.164.0161. arXiv: 1211.5002 [hep-lat].
- [24] Marc Wagner et al. “Scalar mesons and tetraquarks from twisted mass lattice QCD”. In: *Acta Phys. Polon. Supp.* 6.3 (2013). Ed. by Pedro Bicudo et al., pp. 847–852. DOI: 10.5506/APhysPolBSupp.6.847. arXiv: 1302.3389 [hep-lat].
- [25] Masayuki Wakayama et al. “Lattice QCD study of four-quark components of the isosinglet scalar mesons: Significance of disconnected diagrams”. In: *Phys. Rev. D* 91.9 (2015), p. 094508. DOI: 10.1103/PhysRevD.91.094508. arXiv: 1412.3909 [hep-lat].
- [26] Abdou Abdel-Rehim et al. “Investigating efficient methods for computing four-quark correlation functions”. In: *Comput. Phys. Commun.* 220 (2017), pp. 97–121. DOI: 10.1016/j.cpc.2017.06.021. arXiv: 1701.07228 [hep-lat].
- [27] Constantia Alexandrou et al. “Lattice QCD investigation of the structure of the  $a_0(980)$  meson”. In: *Phys. Rev. D* 97.3 (2018), p. 034506. DOI: 10.1103/PhysRevD.97.034506. arXiv: 1711.09815 [hep-lat].
- [28] Anthony Francis et al. “Evidence for charm-bottom tetraquarks and the mass dependence of heavy-light tetraquark states from lattice QCD”. In: *Phys. Rev. D* 99.5 (2019), p. 054505. DOI: 10.1103/PhysRevD.99.054505. arXiv: 1810.10550 [hep-lat].
- [29] R. J. Hudspith et al. “A lattice investigation of exotic tetraquark channels”. In: *Phys. Rev. D* 102 (2020), p. 114506. DOI: 10.1103/PhysRevD.102.114506. arXiv: 2006.14294 [hep-lat].
- [30] Martin Pflaumer et al. “Existence and Non-Existence of Doubly Heavy Tetraquark Bound States”. In: *PoS LATTICE2021* (2022), p. 392. DOI: 10.22323/1.396.0392. arXiv: 2108.10704 [hep-lat].
- [31] Nilmani Mathur and M. Padmanath. “ $\bar{b}c q_1 q_2$  four-quark states from Lattice QCD”. In: *PoS LATTICE2021* (2022), p. 443. DOI: 10.22323/1.396.0443. arXiv: 2111.01147 [hep-lat].
- [32] Marc Wagner et al. “Lattice QCD study of antiheavy-antiheavy-light-light tetraquarks based on correlation functions with scattering interpolating operators both at the source and at the sink”. In: *PoS LATTICE2022* (2023), p. 270. DOI: 10.22323/1.430.0270. arXiv: 2210.09281 [hep-lat].
- [33] Martin Pflaumer et al. “Antiheavy-antiheavy-light-light four-quark bound states”. In: *PoS LATTICE2022* (2023), p. 075. DOI: 10.22323/1.430.0075. arXiv: 2211.00951 [hep-lat].
- [34] Mitja Sadl et al. “Charmonium-like states with  $J^P = 1^+$  and isospin 1”. In: *PoS LATTICE2022* (2023), p. 080. DOI: 10.22323/1.430.0080. arXiv: 2212.04835 [hep-lat].
- [35] Takafumi Aoki, Sinya Aoki, and Takashi Inoue. “Lattice study on a tetraquark state  $T_{bb}$  in the HAL QCD method”. In: *Phys. Rev. D* 108.5 (2023), p. 054502. DOI: 10.1103/PhysRevD.108.054502. arXiv: 2306.03565 [hep-lat].
- [36] M. Padmanath, Archana Radhakrishnan, and Nilmani Mathur. “Bound isoscalar axial-vector  $bc\bar{u}\bar{d}$  tetraquark  $T_{bc}$  in QCD”. In: (July 2023). arXiv: 2307.14128 [hep-lat].
- [37] Constantia Alexandrou et al. “ $\bar{b}b\bar{u}d$  and  $\bar{b}b\bar{u}s$  tetraquarks from lattice QCD using symmetric correlation matrices with both local and scattering interpolating operators”. In: (Apr. 2024). arXiv: 2404.03588 [hep-lat].
- [38] Jorge Segovia. “Effective field theory investigations of the XYZ puzzle”. In: *J. Phys. Conf. Ser.* 742.1 (2016). Ed. by Marco Destefanis et al., p. 012005. DOI: 10.1088/1742-6596/742/1/012005. arXiv: 1603.08527 [hep-ph].
- [39] Jaume Tarrús Castellà. “Heavy hybrids and tetraquarks in effective field theory”. In: *EPJ Web Conf.* 202 (2019). Ed. by A. Bondar and S. Eidelman, p. 01005. DOI: 10.1051/epjconf/201920201005. arXiv: 1901.09761 [hep-ph].

- [40] Bo Wang, Lu Meng, and Shi-Lin Zhu. “Molecular tetraquarks and pentaquarks in chiral effective field theory”. In: *Nucl. Part. Phys. Proc.* 324-329 (2023), pp. 45–48. DOI: 10.1016/j.nuclphysbps.2023.01.010. arXiv: 2210.08227 [hep-ph].
- [41] Chi-Keung Chow. “Semileptonic decays of heavy tetraquarks”. In: *Phys. Rev. D* 51 (1995), pp. 3541–3543. DOI: 10.1103/PhysRevD.51.3541. arXiv: hep-ph/9411221.
- [42] Chun-Yu Cui, Yong-Lu Liu, and Ming-Qiu Huang. “Investigating different structures of the  $Z_b(10610)$  and  $Z_b(10650)$ ”. In: *Phys. Rev. D* 85 (2012), p. 074014. DOI: 10.1103/PhysRevD.85.074014. arXiv: 1107.1343 [hep-ph].
- [43] Raphael M. Albuquerque, Marina Nielsen, and Romulo Rodrigues da Silva. “Exotic  $1^{--}$  States in QCD Sum Rules”. In: *Phys. Rev. D* 84 (2011), p. 116004. DOI: 10.1103/PhysRevD.84.116004. arXiv: 1110.2113 [hep-ph].
- [44] Walter Heupel, Gernot Eichmann, and Christian S. Fischer. “Tetraquark Bound States in a Bethe-Salpeter Approach”. In: *Phys. Lett. B* 718 (2012), pp. 545–549. DOI: 10.1016/j.physletb.2012.11.009. arXiv: 1206.5129 [hep-ph].
- [45] Woosung Park and Su Houng Lee. “Color spin wave functions of heavy tetraquark states”. In: *Nucl. Phys. A* 925 (2014), pp. 161–184. DOI: 10.1016/j.nuclphysa.2014.02.008. arXiv: 1311.5330 [nucl-th].
- [46] Thomas D. Cohen and Richard F. Lebed. “Tetraquarks with exotic flavor quantum numbers at large  $N_c$  in QCD(AS)”. In: *Phys. Rev. D* 89.5 (2014), p. 054018. DOI: 10.1103/PhysRevD.89.054018. arXiv: 1401.1815 [hep-ph].
- [47] P. Bicudo and M. Cardoso. “Tetraquark bound states and resonances in the unitary and microscopic triple string flip-flop quark model, the light-light-antiheavy-antiheavy  $qq\bar{Q}\bar{Q}$  case study”. In: *Phys. Rev. D* 94.9 (2016), p. 094032. DOI: 10.1103/PhysRevD.94.094032. arXiv: 1509.04943 [hep-ph].
- [48] Jing Wu et al. “Heavy-flavored tetraquark states with the  $QQ\bar{Q}\bar{Q}$  configuration”. In: *Phys. Rev. D* 97.9 (2018), p. 094015. DOI: 10.1103/PhysRevD.97.094015. arXiv: 1605.01134 [hep-ph].
- [49] S. S. Agaev, K. Azizi, and H. Sundu. “Open charm-bottom scalar tetraquarks and their strong decays”. In: *Phys. Rev. D* 95.3 (2017), p. 034008. DOI: 10.1103/PhysRevD.95.034008. arXiv: 1611.00293 [hep-ph].
- [50] Ciaran Hughes, Estia Eichten, and Christine T. H. Davies. “Searching for beauty-fully bound tetraquarks using lattice nonrelativistic QCD”. In: *Phys. Rev. D* 97.5 (2018), p. 054505. DOI: 10.1103/PhysRevD.97.054505. arXiv: 1710.03236 [hep-lat].
- [51] S. S. Agaev et al. “Stable scalar tetraquark  $T_{bb;\bar{u}\bar{d}}^-$ ”. In: *Eur. Phys. J. A* 56 (2020), p. 177. DOI: 10.1140/epja/s10050-020-00187-9. arXiv: 2001.01446 [hep-ph].
- [52] Eric Braaten, Li-Ping He, and Abhishek Mohapatra. “Masses of doubly heavy tetraquarks with error bars”. In: *Phys. Rev. D* 103.1 (2021), p. 016001. DOI: 10.1103/PhysRevD.103.016001. arXiv: 2006.08650 [hep-ph].
- [53] Hong-Fei Zhang and Yan-Qing Ma. “Exploring the di- $J/\psi$  resonances based on \textit{itab} initio perturbative QCD”. In: (Sept. 2020). arXiv: 2009.08376 [hep-ph].
- [54] Pedro Bicudo et al. “Importance of meson-meson and of diquark-antidiquark creation operators for a  $\bar{b}\bar{b}ud$  tetraquark”. In: *Phys. Rev. D* 103.11 (2021), p. 114506. DOI: 10.1103/PhysRevD.103.114506. arXiv: 2101.00723 [hep-lat].
- [55] R. M. Albuquerque et al. “Doubly hidden  $0^{++}$  molecules and tetraquarks states from QCD at NLO”. In: *Nucl. Part. Phys. Proc.* 312-317 (2021), pp. 120–124. DOI: 10.1016/j.nuclphysbps.2021.05.031. arXiv: 2102.08776 [hep-ph].
- [56] Xuejie Liu et al. “The explanation of some exotic states in the  $c\bar{s}\bar{c}\bar{s}$  tetraquark system”. In: *Eur. Phys. J. C* 81.10 (2021), p. 950. DOI: 10.1140/epjc/s10052-021-09752-y. arXiv: 2103.12425 [hep-ph].
- [57] S. S. Agaev, K. Azizi, and H. Sundu. “Newly observed exotic doubly charmed meson  $T_{cc}^+$ ”. In: *Nucl. Phys. B* 975 (2022), p. 115650. DOI: 10.1016/j.nuclphysb.2022.115650. arXiv: 2108.00188 [hep-ph].
- [58] Michael Eichberg and Marc Wagner. “Computation of masses of quarkonium bound states using heavy quark potentials from lattice QCD”. In: *PoS FAIRness2022* (2023), p. 014. DOI: 10.22323/1.419.0014. arXiv: 2208.09337 [hep-lat].
- [59] S. S. Agaev, K. Azizi, and H. Sundu. “Near-threshold structures in the  $D_s+D_s^-$  mass distribution of the decay  $B^+\rightarrow D_s+D_s^-K^+$ ”. In: *Phys. Rev. D* 107.9 (2023), p. 094018. DOI: 10.1103/PhysRevD.107.094018. arXiv: 2303.02457 [hep-ph].
- [60] Pablo G. Ortega, David R. Entem, and Francisco Fernández. “Exploring  $T\psi\psi$  tetraquark candidates in a coupled-channels formalism”. In: *Phys. Rev. D* 108.9 (2023), p. 094023. DOI: 10.1103/PhysRevD.108.094023. arXiv: 2307.00532 [hep-ph].



- [61] Pedro Bicudo and Marc Wagner. “Lattice QCD signal for a bottom-bottom tetraquark”. In: *Phys. Rev. D* 87.11 (2013), p. 114511. DOI: 10.1103/PhysRevD.87.114511. arXiv: 1209.6274 [hep-ph].
- [62] Eric Braaten, Christian Langmack, and D. Hudson Smith. “Born-Oppenheimer Approximation for the XYZ Mesons”. In: *Phys. Rev. D* 90.1 (2014), p. 014044. DOI: 10.1103/PhysRevD.90.014044. arXiv: 1402.0438 [hep-ph].
- [63] Pedro Bicudo, Jonas Scheunert, and Marc Wagner. “Including heavy spin effects in the prediction of a  $\bar{b}bud$  tetraquark with lattice QCD potentials”. In: *Phys. Rev. D* 95.3 (2017), p. 034502. DOI: 10.1103/PhysRevD.95.034502. arXiv: 1612.02758 [hep-lat].
- [64] Pedro Bicudo et al. “ $ud\bar{b}\bar{b}$  tetraquark resonances with lattice QCD potentials and the Born-Oppenheimer approximation”. In: *Phys. Rev. D* 96.5 (2017), p. 054510. DOI: 10.1103/PhysRevD.96.054510. arXiv: 1704.02383 [hep-lat].
- [65] Pedro Bicudo et al. “Tetraquark resonances computed with static lattice QCD potentials and scattering theory”. In: *EPJ Web Conf.* 175 (2018). Ed. by M. Della Morte et al., p. 05017. DOI: 10.1051/epjconf/201817505017. arXiv: 1711.08830 [hep-lat].
- [66] Joan Soto and Jaume Tarrús Castellà. “Nonrelativistic effective field theory for heavy exotic hadrons”. In: *Phys. Rev. D* 102.1 (2020), p. 014012. DOI: 10.1103/PhysRevD.102.014012. arXiv: 2005.00552 [hep-ph].
- [67] Pedro Bicudo et al. “Computation of the quarkonium and meson-meson composition of the  $\Upsilon(nS)$  states and of the new  $\Upsilon(10753)$  Belle resonance from lattice QCD static potentials”. In: *Phys. Rev. D* 103.7 (2021), p. 074507. DOI: 10.1103/PhysRevD.103.074507. arXiv: 2008.05605 [hep-lat].
- [68] Lasse Mueller et al. “Bottomonium resonances from lattice QCD static-static-light-light potentials”. In: *PoS LATTICE2021* (2022), p. 349. DOI: 10.22323/1.396.0349. arXiv: 2108.08100 [hep-lat].
- [69] Jakob Hoffmann, André Zimmermann-Santos, and Marc Wagner. “Inclusion of heavy spin effects in the  $ud\bar{b}\bar{b}$   $I(J^P)=0(1^-)$  four-quark channel in the Born-Oppenheimer approximation”. In: *PoS LATTICE2022* (2023), p. 262. DOI: 10.22323/1.430.0262. arXiv: 2211.15765 [hep-lat].
- [70] Pedro Bicudo et al. “Study of  $I=0$  bottomonium bound states and resonances in S, P, D, and F waves with lattice QCD static-static-light-light potentials”. In: *Phys. Rev. D* 107.9 (2023), p. 094515. DOI: 10.1103/PhysRevD.107.094515. arXiv: 2205.11475 [hep-lat].
- [71] Luciano Maiani et al. “Doubly heavy tetraquarks in the Born-Oppenheimer approximation”. In: *Phys. Lett. B* 836 (2023), p. 137624. DOI: 10.1016/j.physletb.2022.137624. arXiv: 2208.02730 [hep-ph].
- [72] Pedro Bicudo et al. “BB interactions with static bottom quarks from Lattice QCD”. In: *Phys. Rev. D* 93.3 (2016), p. 034501. DOI: 10.1103/PhysRevD.93.034501. arXiv: 1510.03441 [hep-lat].
- [73] Antje Peters et al. “Investigation of  $B\bar{B}$  four-quark systems using lattice QCD”. In: *J. Phys. Conf. Ser.* 742.1 (2016). Ed. by Marco Destefanis et al., p. 012006. DOI: 10.1088/1742-6596/742/1/012006. arXiv: 1602.07621 [hep-lat].
- [74] Travis Whyte, David J. Wilson, and Christopher E. Thomas. “Near-threshold states in coupled  $DD^* - D^*D^*$  scattering from lattice QCD”. In: (May 2024). arXiv: 2405.15741 [hep-lat].
- [75] Archana Radhakrishnan, M. Padmanath, and Nilmani Mathur. “Isoscalar axial-vector bottom-charm tetraquarks from QCD”. In: *Nuovo Cim. C* 47.4 (2024), p. 168. DOI: 10.1393/ncc/i2024-24168-x.
- [76] Mitja Sadl et al. “Charmoniumlike Channels  $1^+$  with Isospin 1 from Lattice and Effective Field Theory”. In: (June 2024). arXiv: 2406.09842 [hep-lat].
- [77] Sara Collins et al. “Toward the quark mass dependence of  $T_{cc}^+$  from lattice QCD”. In: *Phys. Rev. D* 109.9 (2024), p. 094509. DOI: 10.1103/PhysRevD.109.094509. arXiv: 2402.14715 [hep-lat].
- [78] Yan Lyu et al. “Doubly charmed tetraquark  $T_{cc}^+$  in (2+1)-flavor QCD near physical point”. In: *PoS LATTICE2023* (2024), p. 077. DOI: 10.22323/1.453.0077. arXiv: 2401.13917 [hep-lat].
- [79] Emmanuel Ortiz-Pacheco et al. “Doubly charmed tetraquark: isospin channels and diquark-antidiquark interpolators”. In: (Dec. 2023). DOI: 10.22323/1.453.0052. arXiv: 2312.13441 [hep-lat].
- [80] Constantia Alexandrou et al. “Shallow Bound States and Hints for Broad Resonances with Quark Content  $b^-c^-ud$  in  $B-D^-$  and  $B^*-D^-$  Scattering from Lattice QCD”. In: *Phys. Rev. Lett.* 132.15 (2024), p. 151902. DOI: 10.1103/PhysRevLett.132.151902. arXiv: 2312.02925 [hep-lat].
- [81] Kenneth G. Wilson. “Confinement of Quarks”. In: *Phys. Rev. D* 10 (1974). Ed. by J. C. Taylor, pp. 2445–2459. DOI: 10.1103/PhysRevD.10.2445.
- [82] Rajendra D. Jain. “The form factors for the rare decay  $B \rightarrow K\ell^+\ell^-$  from three-flavor lattice QCD”. In: *PoS LAT2006* (2006). Ed. by Tom Blum et al., p. 085. DOI: 10.22323/1.032.0085.
- [83] C. Alexandrou et al. “The Nucleon electromagnetic form factors from Lattice QCD”. In: *Phys. Rev. D* 74 (2006), p. 034508. DOI: 10.1103/PhysRevD.74.034508. arXiv: hep-lat/0605017.

- [84] Takeshi Yamazaki et al. “Nucleon form factors with 2+1 flavor dynamical domain-wall fermions”. In: *Phys. Rev. D* 79 (2009), p. 114505. DOI: 10.1103/PhysRevD.79.114505. arXiv: 0904.2039 [hep-lat].
- [85] S. Aoki et al. “Pion form factors from two-flavor lattice QCD with exact chiral symmetry”. In: *Phys. Rev. D* 80 (2009), p. 034508. DOI: 10.1103/PhysRevD.80.034508. arXiv: 0905.2465 [hep-lat].
- [86] J. Koponen, C. T. H. Davies, and G. Donald. “D to K and D to pi semileptonic form factors from Lattice QCD”. In: *5th International Workshop on Charm Physics*. Aug. 2012. arXiv: 1208.6242 [hep-lat].
- [87] William Detmold et al. “Form factors for  $\Lambda_b \rightarrow \Lambda$  transitions from lattice QCD”. In: *PoS LATTICE2012* (2012). Ed. by Derek Leinweber et al., p. 123. DOI: 10.22323/1.164.0123. arXiv: 1211.5127 [hep-lat].
- [88] C. Alexandrou et al. “Nucleon form factors and moments of generalized parton distributions using  $N_f = 2 + 1 + 1$  twisted mass fermions”. In: *Phys. Rev. D* 88.1 (2013), p. 014509. DOI: 10.1103/PhysRevD.88.014509. arXiv: 1303.5979 [hep-lat].
- [89] William Detmold et al. “ $\Lambda_b \rightarrow p\ell^-\bar{\nu}_\ell$  form factors from lattice QCD with static b quarks”. In: *Phys. Rev. D* 88.1 (2013), p. 014512. DOI: 10.1103/PhysRevD.88.014512. arXiv: 1306.0446 [hep-lat].
- [90] Chris Bouchard et al. “Rare decay  $B \rightarrow K\ell^+\ell^-$  form factors from lattice QCD”. In: *Phys. Rev. D* 88.5 (2013). [Erratum: *Phys.Rev.D* 88, 079901 (2013)], p. 054509. DOI: 10.1103/PhysRevD.88.054509. arXiv: 1306.2384 [hep-lat].
- [91] Ronald R. Horgan et al. “Lattice QCD calculation of form factors describing the rare decays  $B \rightarrow K^*\ell^+\ell^-$  and  $B_s \rightarrow \phi\ell^+\ell^-$ ”. In: *Phys. Rev. D* 89.9 (2014), p. 094501. DOI: 10.1103/PhysRevD.89.094501. arXiv: 1310.3722 [hep-lat].
- [92] P. E. Shanahan et al. “Electric form factors of the octet baryons from lattice QCD and chiral extrapolation”. In: *Phys. Rev. D* 90 (2014), p. 034502. DOI: 10.1103/PhysRevD.90.034502. arXiv: 1403.1965 [hep-lat].
- [93] Daping Du et al. “ $B \rightarrow \pi\ell\nu$  semileptonic form factors from unquenched lattice QCD and determination of  $|V_{ub}|$ ”. In: *PoS LATTICE2014* (2014), p. 385. DOI: 10.22323/1.214.0385. arXiv: 1411.6038 [hep-lat].
- [94] C. Alexandrou et al. “Proton and neutron electromagnetic form factors from lattice QCD”. In: *Phys. Rev. D* 100.1 (2019), p. 014509. DOI: 10.1103/PhysRevD.100.014509. arXiv: 1812.10311 [hep-lat].
- [95] Sungwoo Park et al. “Precision nucleon charges and form factors using (2+1)-flavor lattice QCD”. In: *Phys. Rev. D* 105.5 (2022), p. 054505. DOI: 10.1103/PhysRevD.105.054505. arXiv: 2103.05599 [hep-lat].
- [96] Stefan Meinel and Gumaro Rendon. “ $\Lambda_b \rightarrow \Lambda_c^*(2595, 2625)\ell^-\bar{\nu}$  form factors from lattice QCD”. In: *Phys. Rev. D* 103.9 (2021), p. 094516. DOI: 10.1103/PhysRevD.103.094516. arXiv: 2103.08775 [hep-lat].
- [97] Jonathan Lozano et al. “Resonance form factors from finite-volume correlation functions with the external field method”. In: *JHEP* 10 (2022), p. 106. DOI: 10.1007/JHEP10(2022)106. arXiv: 2205.11316 [hep-lat].
- [98] C. Alexandrou et al. “Nucleon electromagnetic form factors using  $N_f=2+1+1$  twisted mass fermion ensembles at the physical mass point”. In: *PoS LATTICE2022* (2023), p. 114. DOI: 10.22323/1.430.0114.
- [99] J. M. Flynn et al. “Exclusive semileptonic  $B_s \rightarrow K\ell\nu$  decays on the lattice”. In: *Phys. Rev. D* 107.11 (2023), p. 114512. DOI: 10.1103/PhysRevD.107.114512. arXiv: 2303.11280 [hep-lat].
- [100] Daniel C. Hackett et al. “Gravitational form factors of the pion from lattice QCD”. In: *Phys. Rev. D* 108.11 (2023), p. 114504. DOI: 10.1103/PhysRevD.108.114504. arXiv: 2307.11707 [hep-lat].
- [101] Martin J. Savage. “Nuclear physics and lattice QCD”. In: *PoS LAT2005* (2006). Ed. by Christopher Michael, p. 020. DOI: 10.22323/1.020.0020. arXiv: hep-lat/0509048.
- [102] Dru Bryant Renner et al. “Calculation of the nucleon axial charge in lattice QCD”. In: *J. Phys. Conf. Ser.* 46 (2006). Ed. by William M. Tang, pp. 152–156. DOI: 10.1088/1742-6596/46/1/021. arXiv: hep-lat/0607008.
- [103] S. R. Beane et al. “Nuclear Physics from Lattice QCD”. In: *Prog. Part. Nucl. Phys.* 66 (2011), pp. 1–40. DOI: 10.1016/j.ppnp.2010.08.002. arXiv: 1004.2935 [hep-lat].
- [104] P. E. Shanahan et al. “Determination of the strange nucleon form factors”. In: *Phys. Rev. Lett.* 114.9 (2015), p. 091802. DOI: 10.1103/PhysRevLett.114.091802. arXiv: 1403.6537 [hep-lat].
- [105] Jiunn-Wei Chen et al. “Nucleon Helicity and Transversity Parton Distributions from Lattice QCD”. In: *Nucl. Phys. B* 911 (2016), pp. 246–273. DOI: 10.1016/j.nuclphysb.2016.07.033. arXiv: 1603.06664 [hep-ph].

- [106] Tanmoy Bhattacharya et al. “Axial, Scalar and Tensor Charges of the Nucleon from 2+1+1-flavor Lattice QCD”. In: *Phys. Rev. D* 94.5 (2016), p. 054508. DOI: 10.1103/PhysRevD.94.054508. arXiv: 1606.07049 [hep-lat].
- [107] P. E. Shanahan. “Chiral Effective Theory Methods and their Application to the Structure of Hadrons from Lattice QCD”. In: *J. Phys. G* 43.12 (2016), p. 124001. DOI: 10.1088/0954-3899/43/12/124001. arXiv: 1606.08812 [hep-lat].
- [108] Martin J. Savage et al. “Axial-Current Matrix Elements in Light Nuclei from Lattice QCD”. In: *PoS ICHEP2016* (2016), p. 506. DOI: 10.22323/1.282.0506. arXiv: 1611.00344 [hep-lat].
- [109] Michael L. Wagman and Martin J. Savage. “Statistics of baryon correlation functions in lattice QCD”. In: *Phys. Rev. D* 96.11 (2017), p. 114508. DOI: 10.1103/PhysRevD.96.114508. arXiv: 1611.07643 [hep-lat].
- [110] Frank Winter et al. “First lattice QCD study of the gluonic structure of light nuclei”. In: *Phys. Rev. D* 96.9 (2017), p. 094512. DOI: 10.1103/PhysRevD.96.094512. arXiv: 1709.00395 [hep-lat].
- [111] Ning Li et al. “Neutron-proton scattering with lattice chiral effective field theory at next-to-next-to-next-to-leading order”. In: *Phys. Rev. C* 98.4 (2018), p. 044002. DOI: 10.1103/PhysRevC.98.044002. arXiv: 1806.07994 [nucl-th].
- [112] Yin Lin et al. “Nucleon mass with highly improved staggered quarks”. In: *Phys. Rev. D* 103.3 (2021), p. 034501. DOI: 10.1103/PhysRevD.103.034501. arXiv: 1911.12256 [hep-lat].
- [113] William Detmold et al. “Lattice QCD Constraints on the Parton Distribution Functions of  ${}^3\text{He}$ ”. In: *Phys. Rev. Lett.* 126.20 (2021), p. 202001. DOI: 10.1103/PhysRevLett.126.202001. arXiv: 2009.05522 [hep-lat].
- [114] Jing Song et al. “ ${}^3\text{S}_1$ - ${}^3\text{D}_1$  coupled channel  $\Lambda_c$  N interactions: chiral effective field theory versus lattice QCD”. In: *Commun. Theor. Phys.* 75.1 (2023), p. 015202. DOI: 10.1088/1572-9494/ac9a3d. arXiv: 2104.02380 [hep-ph].
- [115] Saman Amarasinghe et al. “Variational study of two-nucleon systems with lattice QCD”. In: *Phys. Rev. D* 107.9 (2023), p. 094508. DOI: 10.1103/PhysRevD.107.094508. arXiv: 2108.10835 [hep-lat].
- [116] Xiangkai Sun et al. “Finite-volume pionless effective field theory for few-nucleon systems with differentiable programming”. In: *Phys. Rev. D* 105.7 (2022), p. 074508. DOI: 10.1103/PhysRevD.105.074508. arXiv: 2202.03530 [nucl-th].
- [117] Zohreh Davoudi et al. “Long-distance nuclear matrix elements for neutrinoless double-beta decay from lattice QCD”. In: *Phys. Rev. D* 109.11 (2024), p. 114514. DOI: 10.1103/PhysRevD.109.114514. arXiv: 2402.09362 [hep-lat].
- [118] Ryan Abbott et al. “QCD constraints on isospin-dense matter and the nuclear equation of state”. In: (June 2024). arXiv: 2406.09273 [hep-lat].
- [119] Maxwell T. Hansen and Stephen R. Sharpe. “Multiple-channel generalization of Lellouch-Lüscher formula”. In: *Phys. Rev. D* 86 (2012), p. 016007. DOI: 10.1103/PhysRevD.86.016007. arXiv: 1204.0826 [hep-lat].
- [120] Maxwell T. Hansen and Stephen R. Sharpe. “Relativistic, model-independent, three-particle quantization condition”. In: *Phys. Rev. D* 90.11 (2014), p. 116003. DOI: 10.1103/PhysRevD.90.116003. arXiv: 1408.5933 [hep-lat].
- [121] Maxwell T. Hansen and Stephen R. Sharpe. “Expressing the three-particle finite-volume spectrum in terms of the three-to-three scattering amplitude”. In: *Phys. Rev. D* 92.11 (2015), p. 114509. DOI: 10.1103/PhysRevD.92.114509. arXiv: 1504.04248 [hep-lat].
- [122] Tyler D. Blanton, Fernando Romero-López, and Stephen R. Sharpe. “Implementing the three-particle quantization condition including higher partial waves”. In: *JHEP* 03 (2019), p. 106. DOI: 10.1007/JHEP03(2019)106. arXiv: 1901.07095 [hep-lat].
- [123] Maxwell T. Hansen, Fernando Romero-López, and Stephen R. Sharpe. “Generalizing the relativistic quantization condition to include all three-pion isospin channels”. In: *JHEP* 07 (2020). [Erratum: *JHEP* 02, 014 (2021)], p. 047. DOI: 10.1007/JHEP07(2020)047. arXiv: 2003.10974 [hep-lat].
- [124] Tyler D. Blanton and Stephen R. Sharpe. “Three-particle finite-volume formalism for  $\pi+\pi+K+$  and related systems”. In: *Phys. Rev. D* 104.3 (2021), p. 034509. DOI: 10.1103/PhysRevD.104.034509. arXiv: 2105.12094 [hep-lat].
- [125] Zachary T. Draper et al. “Three relativistic neutrons in a finite volume”. In: *JHEP* 07 (2023), p. 226. DOI: 10.1007/JHEP07(2023)226. arXiv: 2303.10219 [hep-lat].
- [126] Zachary T. Draper and Stephen R. Sharpe. “Three-particle formalism for multiple channels: the  $\eta\pi\pi + K\bar{K}\pi$  system in isosymmetric QCD”. In: *JHEP* 07 (2024), p. 083. DOI: 10.1007/JHEP07(2024)083. arXiv: 2403.20064 [hep-ph].

- [127] David J. Gross and Frank Wilczek. “Ultraviolet Behavior of Nonabelian Gauge Theories”. In: *Phys. Rev. Lett.* 30 (1973). Ed. by J. C. Taylor, pp. 1343–1346. DOI: 10.1103/PhysRevLett.30.1343.
- [128] Matthias Berwein et al. “One Born–Oppenheimer Effective Theory to rule them all: hybrids, tetraquarks, pentaquarks, doubly heavy baryons and quarkonium”. In: (Aug. 2024). arXiv: 2408.04719 [hep-ph].
- [129] S. Godfrey and Nathan Isgur. “Mesons in a Relativized Quark Model with Chromodynamics”. In: *Phys. Rev. D* 32 (1985), pp. 189–231. DOI: 10.1103/PhysRevD.32.189.
- [130] Thomas A. DeGrand. “Lattice QCD at the end of 2003”. In: *Int. J. Mod. Phys. A* 19 (2004), pp. 1337–1394. DOI: 10.1142/S0217751X04017574. arXiv: hep-ph/0312241.
- [131] A. Pineda and J. Soto. “Effective field theory for ultrasoft momenta in NRQCD and NRQED”. In: *Nucl. Phys. B Proc. Suppl.* 64 (1998). Ed. by Stephan Narison, pp. 428–432. DOI: 10.1016/S0920-5632(97)01102-X. arXiv: hep-ph/9707481.
- [132] Nora Brambilla. *pNRQCD: concepts and applications*. 2000. arXiv: hep-ph/0008279 [hep-ph]. URL: <https://arxiv.org/abs/hep-ph/0008279>.
- [133] P. A. Zyla et al. “Review of Particle Physics”. In: *PTEP* 2020.8 (2020), p. 083C01. DOI: 10.1093/ptep/ptaa104.
- [134] G. Breit and E. Wigner. “Capture of Slow Neutrons”. In: *Phys. Rev.* 49 (1936), pp. 519–531. DOI: 10.1103/PhysRev.49.519.
- [135] S. Navas et al. “Review of particle physics”. In: *Phys. Rev. D* 110.3 (2024), p. 030001. DOI: 10.1103/PhysRevD.110.030001.
- [136] Wolfgang Kilian and Thomas Mannel. “QCD corrected  $1/m$  contributions to  $BB$ -mixing”. In: *Physics Letters B* 301.4 (1993), pp. 382–392. DOI: 10.1016/0370-2693(93)91167-1. URL: <https://doi.org/10.1016%2F0370-2693%2893%2991167-1>.
- [137] Matthias Neubert. “Heavy-quark symmetry”. In: *Physics Reports* 245.5-6 (1994), pp. 259–395. DOI: 10.1016/0370-1573(94)90091-4. URL: <https://doi.org/10.1016%2F0370-1573%2894%2990091-4>.
- [138] Matthias Neubert. *Heavy-Quark Effective Theory*. 1996. arXiv: hep-ph/9610266 [hep-ph].
- [139] Antonio Pineda and Antonio Vairo. “The QCD potential at  $\mathcal{O}(1/m^2)$ : Complete spin dependent and spin independent result”. In: *Phys. Rev. D* 63 (2001). [Erratum: Phys.Rev.D 64, 039902 (2001)], p. 054007. DOI: 10.1103/PhysRevD.64.039902. arXiv: hep-ph/0009145.
- [140] Michael Eichberg and Marc Wagner. “Relativistic corrections to the static potential from generalized Wilson loops at finite flow time”. In: *PoS LATTICE2023* (2024), p. 068. DOI: 10.22323/1.453.0068. arXiv: 2311.06560 [hep-lat].
- [141] Lu Meng et al. “Solving the left-hand cut problem in lattice QCD:  $T_{cc}(3875)^+$  from finite volume energy levels”. In: *Phys. Rev. D* 109.7 (2024), p. L071506. DOI: 10.1103/PhysRevD.109.L071506. arXiv: 2312.01930 [hep-lat].
- [142] André Baião Raposo and Maxwell T. Hansen. “Finite-volume scattering on the left-hand cut”. In: (Nov. 2023). arXiv: 2311.18793 [hep-lat].
- [143] Maxwell T. Hansen, Fernando Romero-López, and Stephen R. Sharpe. “Incorporating  $DD\pi$  effects and left-hand cuts in lattice QCD studies of the  $T_{cc}(3875)^+$ ”. In: (Jan. 2024). arXiv: 2401.06609 [hep-lat].